ABSTRACT

Title of dissertation: INTERACTION BETWEEN THE AEROSOL DIRECT EFFECT IN THE LOWER TROPOSPHERE AND THE PLANETARY BOUNDARY LAYER DEPTH

Virginia Ruth Sawyer, Doctor of Philosophy, 2015

Dissertation directed by: Professor Zhanqing Li
Department of Atmospheric and Oceanic Science/Earth System Science Interdisciplinary Center

The planetary boundary layer (PBL) limits the vertical mixing of aerosol emitted to the lower troposphere. The PBL depth and its change over time affect weather, surface air quality and radiative forcing. While model simulations have suggested that the column optical properties of aerosol are associated with changes in the PBL depth in turn, there are few long-term measurements of PBL depth with which to validate the theory. Of the existing methods to detect the PBL depth from atmospheric profiles, many require supporting information from multiple instruments or cannot adapt to changing atmospheric conditions. This study combines two common methods for PBL depth detection (wavelet covariance and iterative curve-fitting) in order to produce more reliable PBL depths for micropulse lidar backscatter (MPL). The combined algorithm is also flexible enough to use with radiosonde and atmospheric emitted radiance interferometer *(*AERI) data.

PBL depth retrievals from these three instruments collected at the Atmospheric Radiation Measurement (ARM) Southern Great Plains (SGP) site are compared to one another to show the robustness of the algorithm. The comparisons were made for different times of day, four seasons, and variable sky conditions. While considerable uncertainties exist in PBL detection using all three types of measurements, the agreement among the PBL products is promising, and the different measurements have complementary advantages. The best agreement in the seasonal cycle occurs in winter, and the best agreement in the diurnal cycle when the boundary-layer regime is mature and changes slowly. PBL depths from instruments with higher temporal resolution (MPL and AERI) are of comparable accuracy to radiosonde-derived PBL depths.

The new PBL depth measurements for SGP are compared to MPL-derived PBL depths from a multiyear lidar deployment at the Hefei Radiation Observatory (HeRO), and the column aerosol optical depth (AOD) for each site is considered. A one-month period at SGP is also modeled to relate AOD to PBL depth. These comparisons show a weak inverse relationship between AOD and daytime PBL depth. This is consistent with predictions that aerosol suppresses surface convection and causes shallower PBLs.

INTERACTION BETWEEN THE AEROSOL DIRECT EFFECT IN THE LOWER TROPOSPHERE AND THE PLANETARY BOUNDARY LAYER DEPTH

by

Virginia Ruth Sawyer

Dissertation submitted to the Faculty of the Graduate School of the
University of Maryland, College Park in partial fulfillment
of the requirements for the degree of
Doctor of Philosophy
2015

Advisory Committee:

Professor Zhanqing Li, Chair
Professor Russell R. Dickerson
Professor Derrick J. Lampkin
Professor Rachel Pinker
Dr. Ellsworth J. Welton
Professor George Hurtt, Dean's Representative

ACKNOWLEDGMENTS

First of all, I'd like to thank my advisor, Dr. Zhanqing Li, for all his help, support and constructive criticism throughout my time at the University of Maryland. This work could not have proceeded without the additional help of Dr. Zhenzhu Wang and Dong Liu at the Key Laboratory of Atmospheric Composition and Optical Radiation, Anhui Institute of Optics and Fine Mechanics, Chinese Academy of Sciences, who graciously guided me through the use of their data; Jianping Guo, who analyzed additional data using my algorithm; and Dr. Shuyan Liu at the University of Maryland, College Park, who provided important insights along with the results she graciously allowed me to borrow.

This project also uses data from the Atmospheric Radiation Measurement (ARM) Program sponsored by the U.S. Department of Energy, Office of Science, Office of Biological and Environmental Research, Climate and Environmental Sciences Division. I'd like to thank Dr. Chitra Sivaraman and other members of the PBL interest group for their encouragement.

Finally, thanks to my husband, Rustom, and to my family and friends. None of this would be possible without their love and moral support.

TABLE OF CONTENTS

LIST OF FIGURES

LIST OF ABBREVIATIONS AND SYMBOLS

θ_v	Virtual potential temperature
ACM2	Asymmetric convective model, version 2; a PBL scheme for WRF-Chem
AERI	Atmospheric emitted radiance interferometer
ARM	Atmospheric Radiation Measurement (US Department of Energy)
AOD	Aerosol optical depth
CBL	Convective boundary layer
CMAQ	Community Multi-scale Air Quality Model
EZD	Entrainment zone depth
HeRO	Hefei Radiation Observatory (31°52′ N, 117°17′E)
LLJ	Low-level jet
MODIS	Moderate Resolution Imaging Spectroradiometer
MFRSR	Multifilter rotating shadowband radiometer
MPL	Micropulse lidar
MPLNET	Micropulse Lidar Network (NASA)
NCP	North China Plain
NIMFR	Normal incidence multifilter radiometer
PBL	Planetary boundary layer
PRD	Pearl River Delta
RL	Residual layer
SASHE	Shortwave array spectroradiometer – hemispheric
SBL	Stable boundary layer
SCB	Sichuan Basin

SGP	Southern Great Plains site (36°36'18.0" N, 97°29'6.0" W)
SSA	Single-scattering albedo
TKE	Turbulent kinetic energy
WRF-Chem	Weather Research and Forecasting model coupled with Chemistry
YRD	Yangtze River Delta
YSU	Yonsei University scheme; a PBL scheme for WRF-Chem

Chapter 1. Background

1.1 The Planetary Boundary Layer

The planetary boundary layer (PBL) is the part of the lower troposphere in direct contact with the surface, ranging from several hundred meters to a few kilometers in depth. It may be defined in terms of thermodynamics or in terms of turbulent mixing; the mixed layer below the PBL top is distinguishable from the free troposphere by differences in temperature and stability as well as turbulent flow. The difference in chemical content may be the most important, however, because of its impact on surface air quality [*Seinfeld and Pandis*, 2006]. The PBL depth defines a finite but varying volume into which pollutants can disperse.

Changes in the depth of the PBL over time follow several different processes, the most important of which over land is the diurnal cycle in radiative surface heating. Under typical conditions, the PBL grows deeper in response to rising temperatures through the morning, peaks in the afternoon or early evening, and collapses after sunset [*Stull*, 1988]. The PBL top may rise as high as 5 km in extreme cases of clear-sky convection [*Ma et al.*, 2011]. If insolation stops during the day, as during the solar eclipse observed by *Amiridis et al.* [2007], the PBL top height decreases just as it typically does in the evening. Over the ocean, where strong surface heating is rare, changes in the PBL depth are more often driven by synoptic weather, but may nevertheless occur on time scales of only a few hours.

The most common measurements of thermodynamic profiles are taken by radiosonde. These are launched twice a day operationally, or 4-8 times daily during field experiments [*Seibert et al.*, 2000]. The temporal resolution in radiosonde-derived PBL

data is therefore too sparse to detect the evolution of the diurnal structure. Smaller-scale boundary layer processes and waves are obscured. For many sites in the western hemisphere, operational radiosonde launches also occur during transition times when the PBL is changing rapidly (00UTC and 12UTC) so extremes of the diurnal cycle go unobserved. PBL detection by remote sensing can improve the temporal resolution of the data, usually by using a proxy for the thermodynamic profile. Wind profiling provides some clues about the turbulence structure, so radar wind profilers [*Bianco and Wilczak,* 2002] and sodars are used to detect the PBL under a definition based on turbulence rather than the thermodynamic structure [*Beyrich and Görsdorf*, 1995].

The seasonal cycle echoes the diurnal cycle, with the strongest deep convection in the summer months [e.g., *Liu and Liang,* 2010]. In the winter, changes in the synoptic weather govern the PBL depth and generally lead to shallower PBLs with a weaker diurnal cycle. It is important for any PBL detection method to replicate both the diurnal and seasonal cycles of PBL behavior in order to fully understand its effects on air quality and climate.

1.2 Aerosol and Clouds as Proxy

Buoyant stability restricts the mixing of aerosols through the PBL top to just three mechanisms: deep convection, orographic lifting and transport by warm conveyor belt processes [*Donnell et al.,* 2001; *Twohy et al.,* 2002; *Henne et al.,* 2004; *Ding et al.,* 2009]. Highly polluted airmasses that enter long range transport in these three ways form aerosol plumes that may persist for thousands of kilometers in the middle and upper

troposphere. In the Arctic, where there are few local sources, long range transport of aerosol is responsible for intense springtime pollution events [*Law and Stohl*, 2007; *Quinn et al.*, 2007]. By contrast, the mineral dust aerosol that enters long range transport during Asian dust events continues to interact with urban aerosols emitted downstream, and may not be easily distinguishable from mixed-layer aerosol [e.g., *Li et al.*, 2010; *Sun et al.*, 2010].

However, most aerosols that are emitted within the mixed layer remain there until removal from the atmosphere, usually within a few kilometers of their origin [*Seinfeld and Pandis*, 2006]. The vertical distribution of aerosols through the lower troposphere therefore depends heavily on the depth of the PBL, and the PBL depth can be inferred in turn from the aerosol profile. Several "gradient" methods rely on the drop in aerosol concentration across the boundary in order to detect the PBL top height, defined as the center of a transition zone or inversion at the top of the surface layer.

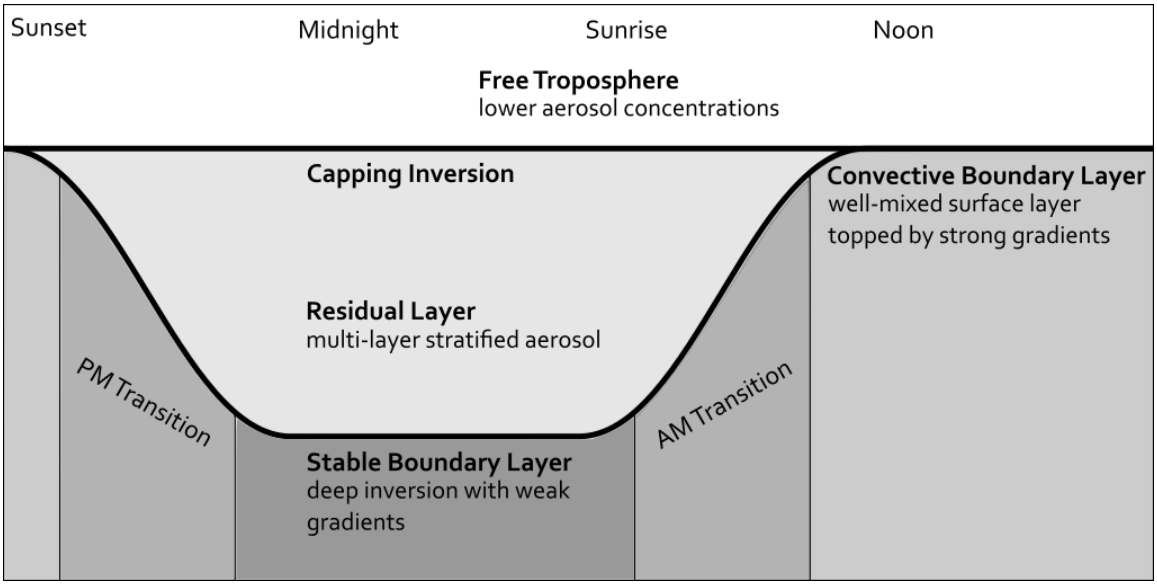

Figure 1.1. Schematic of PBL regimes and transitions, adapted from *Stull* [1988].

Figure 1.1 illustrates the regimes of a typical PBL diurnal cycle, with labels describing their characteristic relative aerosol concentration and structure. During the day, the convective boundary layer (CBL) is well-mixed both thermodynamically and with respect to aerosol content, and is also typically more polluted than the free troposphere above its top [*Melfi et al.,* 1985]. This uniform higher concentration of aerosols is easily detected by aerosol lidar, distinct from the lower and more stratified concentration of aerosol in the free troposphere. At night, much of the aerosol from the CBL of the previous day remains in a residual layer (RL) between the capping inversion and the surface, while a shallow nocturnal inversion—the stable boundary layer (SBL)—forms near the surface in response to radiative cooling. Transition times are defined by the development of the CBL as surface insolation strengthens in the morning, and then by the collapse of the CBL as nightfall cuts off the source of heating.

In addition, the PBL top is often associated with cumulus cloud layers. Figure 1.2 illustrates the various conceptual regimes for cloud layers interacting with the PBL [*Medeiros et al.,* 2005]: whether forming the cloud base of deep convection or the capping inversion inhibiting the growth of stratocumulus, the PBL top is so bound up with cloud processes that the cloud signal in remote sensing can also help determine the PBL depth [*Davis et al.,* 2000]. Therefore gradient methods for PBL detection can potentially work for both clear-sky and cloudy conditions.

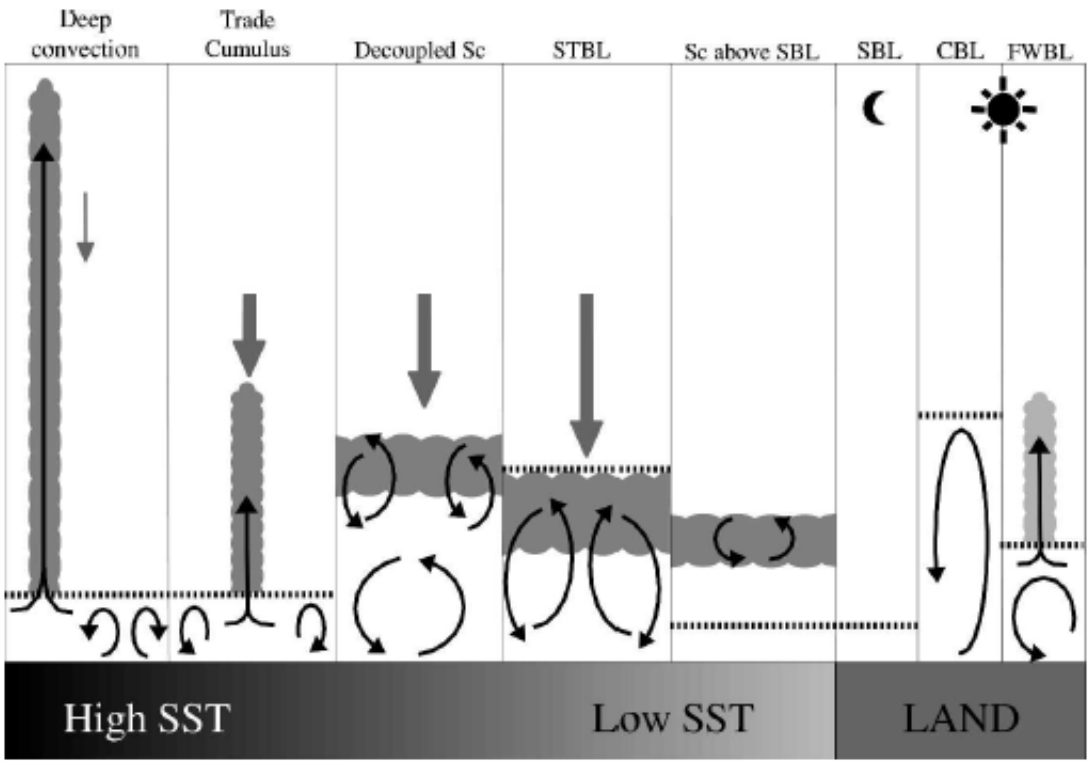

Figure 1.2. From *Medeiros et al.* [2005], PBL regimes by cloud type.

1.3 Modeled Aerosol-PBL Interaction

The aerosol direct effect is the change in heating of the atmosphere caused by direct absorption or scattering of radiation by particulate matter. The integrated column heating by the aerosol direct effect is a major factor in anthropogenic climate change and among the least understood after cloud-aerosol interaction [*IPCC,* 2007]. However, not only the column total heating but also the distribution of radiative effects along the column makes a difference to the climate. *Venkatram and Viskanta* [1977] warned in a simple modeling study that aerosols alter the energy distribution between the surface and the PBL top, increasing the absorption of solar energy in the mixed layer at the expense of heating at the surface. The effect would be a reduction in the CBL depth and greater

atmospheric stability, countered by warming in the lower troposphere that could lead to later convection. Other studies simulated nuclear winter scenarios, and modeled a thick smoke layer at tropopause height. The reduction in surface heating still occurs, but the aerosol-induced heating of the atmosphere occurs at too high an altitude to involve the PBL. *Garratt et al.* [1990] found that under such conditions the maximum CBL depth could be suppressed from 2300 m in the control case to 1650 m at an aerosol optical depth (AOD) of 0.2 and 600 m at an AOD of 1.0. *Yu et al.* [2002] found that such a pronounced effect is highly dependent on the single-scattering albedo (SSA) of the aerosol layer. For the same AOD, the maximum depth of the CBL increased by several hundred meters with each 0.1 decrease in SSA. The simulated CBL began to develop later in the day and collapsed earlier in the evening as the aerosol became less scattering and more absorbing. This suggests that both AOD and SSA affect the maximum depth of the CBL, but that the shape and phase of the PBL diurnal cycle is more sensitive to SSA. Using a single-column chemical transport model, *Park et al.* [2001] found that the suppression of surface convection by the mostly scattering aerosols typical of their eastern US study region impacted the surface air quality not only through the reduced dilution volume available under a shallow PBL, but also by enhancing the production of surface ozone, resulting in further radiative forcing within the PBL. The importance of aerosol to the PBL depth and surface air quality is magnified by its interaction with other atmospheric processes.

More recently, it has been shown that aerosol within the PBL itself may also have a net effect of significantly suppressed convection. *Ding et al.* [2013] found that regional plumes bearing absorbing aerosol, especially from a combination of biomass burning and

fossil fuel combustion, could enhance the stability of the PBL by heating its upper levels at the expense of the surface. The absence of this effect in some forecast models may explain their underestimation of surface air pollution episodes in urban China. The study recommends that forecast models be fully coupled with atmospheric chemistry. Aside from the surface air quality forecast, the changed PBL dynamics have consequences for convective precipitation. As in *Andreae et al.* [2004] and *Feingold et al.* [2005] in their studies of Amazon smoke, suppressed convection delays the onset of precipitation but may lead to later invigoration and intense storms. *Zhang et al.* [2010] used the Weather Research and Forecasting model coupled with Chemistry (WRF-Chem) to investigate the effects of aerosols over the continental U.S. in January and July 2001; the study found that with a reduction of incoming solar radiation of 11.3 W m^{-2} and 39.5 W m^{-2}, respectively, there was a resulting temperature decrease of 0.16-0.37 K and a reduction in PBL depth of 23-24%, compared to the aerosol-free case.

Finally, in a recent presentation at the AMS Annual Meeting, *Xing et al.* [2015] presented results of a simulation using WRF coupled with the Community Multi-scale Air Quality (CMAQ) Model, for the period 1990-2010 in eastern China, the eastern U.S. and Europe. The study predicted that for each 1.0 unit of increased AOD, there is a corresponding decrease of 0.3 to 0.4 K in average surface temperature and a resulting 69 to 79 m decrease in PBL depth: a difference so small that it may be difficult to detect in observations, but with significant climate effects when taken on a continental scale. Because the PBL depth and aerosol loading are subject to many interconnected processes, the effort to quantify the suppression of convection by boundary-layer aerosol is ongoing.

However, models consistently find such a mechanism; accurate observations of the PBL over long time periods in the instrument record should be able to find the same effect.

The stabilization of the PBL by convection suppression exacerbates decreases in overall surface air quality, as periods of stagnation lengthen and the washout by precipitation is limited to less frequent but more intense events. In combination with the projected weakening of global circulation and a decreasing frequency of mid-latitude cyclones due to greenhouse effect-induced climate change [*Jacob and Winner*, 2009] boundary-layer aerosol loading is therefore projected to increase even when emission rates are held constant, a climate penalty for particulate pollution analogous to the penalty by which warmer temperatures increase the formation of tropospheric ozone [e.g., *Bloomer et al.*, 2009; *He et al.*, 2013]. This aerosol climate penalty is driven not by greater formation of aerosols, but by changes in the end of their lifetime in the atmosphere: reduced dilution volume and washout rates, to which the aerosol itself contributes through direct, indirect and semi-direct radiative effects. Models have shown that the health and radiative effects of boundary-layer aerosols are likely to increase in future climates. At polluted sites in China, shallower PBL depths, exacerbated air quality problems and suppressed convective precipitation have already been observed [*Yang et al.*, 2013a,b]. The link to increased aerosol loading must be made explicit.

1.4 Objectives and Outline

The purpose of this dissertation is to investigate whether the predicted suppression of surface convection and PBL depth can be detected in long-term instrument

records. The first step toward this goal is to accurately detect the PBL depth, which requires the development of an algorithm that can operate with minimal human intervention or prior knowledge of atmospheric or instrument conditions, over time series that cover multiple years at high temporal resolution. The second step is to demonstrate that remote sensing of the aerosol distribution with height is an effective measurement to show PBL depth, which can be shown if the resulting PBL depths are comparable to PBL depths reached by other instruments in the same location and time period; in order to eliminate variables and demonstrate the flexibility of the algorithm, the same algorithm can be applied to profiles from each instrument. Because remote sensing is capable of providing much more detailed information about atmospheric structure than the lower-resolution thermodynamic profiles from radiosonde and other sources, the resulting PBL depth retrievals are more representative of actual PBL behavior. Locations with contrasting AOD values can then show the relationship between the PBL depth and AOD, for comparison with model predictions.

Chapter 1 provides an overview of the PBL, its regimes and its relationship to aerosol, and model predictions for the behavior of the PBL in polluted conditions. Chapter 2 lists the sources of data and model output used in this project. Chapter 3 describes methods used to detect the PBL depth and the development of a new algorithm for PBL detection that combines the advantages of its predecessors. Chapter 4 evaluates the reliability of this algorithm by applying it to observations from three types of atmospheric profile. Chapter 5 compares PBL depth results from sites in the U.S. and China. Chapter 6 uses PBL depth results from the two sites with the longest available time series, including results from a modeled PBL scheme, and compares them to column

AOD measurements. Chapter 7 presents a summary of the project, and Chapter 8 suggests approaches for future work.

Chapter 2. Data Sources

2.1 Micropulse Lidar

Micropulse lidar (MPL) [*Spinhirne et al.,* 1995] is the primary instrument used in this project, which relies on the similar configurations of MPL instruments at sites across the globe, including networks such as the Atmospheric Radiation Measurement (ARM) facilities [*Spinhirne,* 1993; *Flynn et al.,* 2007] and NASA's Micropulse Lidar Network (MPLNET) [*Welton et al.*, 2001], in order to make comparisons among their locations. Ground-based, upward-directed lidar are in the best position to observe boundary-layer processes with a maximum signal-to-noise ratio; the use of a single wavelength at 527-532 nm ensures sensitivity to aerosol and cloud layers [*Campbell et al.,* 2002]. MPL offers high temporal resolution compared to radiosonde, while requiring minimal human oversight. As a result, it is able to observe clouds and aerosols on a time scale that matches PBL processes, potentially for many years at a stretch. For these reasons, while the PBL detection algorithm described in a later section is adaptable to multiple atmospheric profile measurements from many different instrument types, it was originally developed for MPL.

The Southern Great Plains site near Ponca City, OK (36°36'18.0" N, 97°29'6.0" W) has included MPL as part of the ARM program measurements since May 1996. A number of changes to the instrument have been made over time, and some significant gaps in the time series exist. The original data set, used for the instrument intercomparison, extends to 2004. Data collected after the lidar was upgraded with a polarization switch in June 2006 [*Coulter*, 2012] are not included in this project. The ten-year time series analyzed here is nevertheless longer than any of the time series available

from MPL deployments in China. The time series includes one attenuated backscatter profile per minute, which is averaged to five-minute intervals for PBL detection. While the vertical resolution of the backscatter data is 75 m, the incomplete overlap between the beam spread and the telescope field of view means that accurate measurements begin at an altitude of approximately 600 m even after correction. After 2006, an error in the overlap correction makes backscatter profiles of the lower troposphere too unreliable to draw conclusions about aerosol content, though the more recent data is available through ARM for the purposes of cloud studies. Cloud attenuation and interference from sunlight limit the upper range of the profile. This study also makes use of cloud base heights determined by the algorithm described in *Wang and Sassen* [2001] and included in the ARM data product for MPL [*Sivaraman and Comstock*, 2011]. While the MPL cloud mask includes information about cloud base and top heights at levels throughout the troposphere, the height of the lowest cloud base is the variable most directly relevant to PBL detection.

In China, the longest MPL deployment used in this study is at the Hefei Radiation Observatory (HeRO; 31°52′ N, 117°17′E), which has data running from 2002 to 2008 [*Wang et al.*, 2014]. Profiles from the HeRO MPL are available on 15-minute intervals, and are analyzed for PBL depth at the same time interval. The overlap correction for the instrument is shallower than at SGP, providing accurate backscatter measurements starting at approximately 400 m altitude. Shorter MPL time series of several months' duration, each with their own resolution and overlap functions, are available from Shouxian (32°35′ N, 116°47′ E) in 2008 and Xianghe (39°45′ N, 116°59′ E) in 2013 (Figure 2.1).

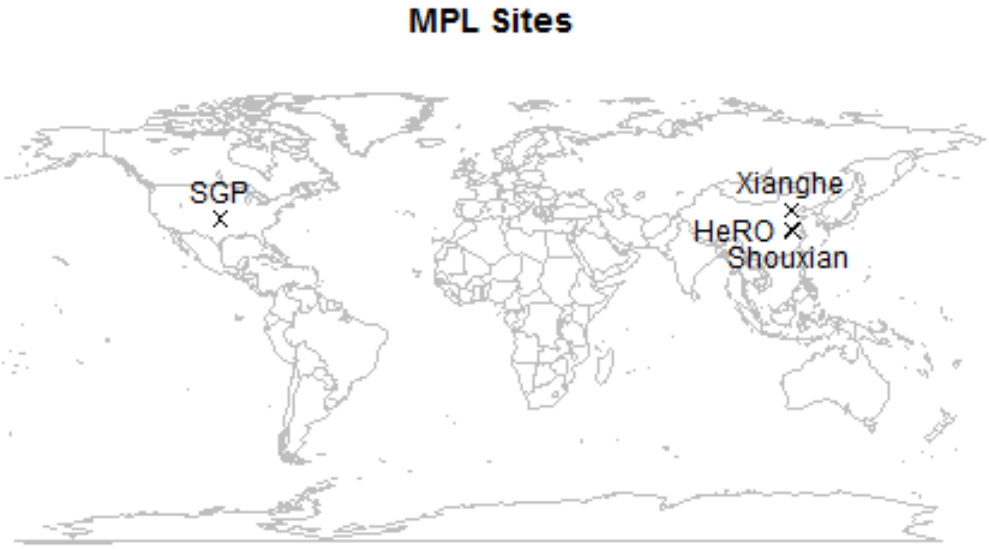

Figure 2.1. Locations of MPL deployments used in this project.

2.2 Thermodynamic Profiles

In order to assess the reliability of the PBL detection algorithm, the project uses profiles from radiosonde and infrared spectrometer taken at the SGP site during the period for which the MPL data is analyzed. ARM radiosonde launches at the site [*Holdridge et al.*, 2011] took place at least four times per day, usually at 00:00, 06:00, 12:00 and 18:00 UTC but also in significant numbers at 03:00, 09:00, 15:00 and 21:00. The multiyear length of the analysis period makes it possible to construct a mean diurnal cycle at three-hour intervals even though no single day had all eight measurements taken. The vertical profile of virtual potential temperature θ_v is calculated from the temperature and relative humidity measurements. While the vertical resolution of the data varies

according to the ascent rate of the balloon, data points within the boundary layer occur approximately 10 m apart.

The atmospheric emitted radiance interferometer (AERI) instrument at SGP can retrieve one θ_v profile every eight minutes [*Feltz et al.,* 1998; *Feltz et al.,* 2003; *Feltz et al.,* 2007]. The high temporal resolution has advantages over radiosonde for the purposes of PBL detection, but the vertical resolution is much lower and varies with altitude. θ_v is retrieved every 50 m at the surface but by 500 m, retrievals are made at 500-m intervals. At the top of the profile, the resolution is 2 km. Another disadvantage compared to radiosonde is that AERI cannot make reliable measurements of the temperature and moisture within a cloud layer; profiles with clouds in or near the boundary layer must be excluded from analysis. AERI retrievals are available from June 1996 to the present, with a change to the data format in 2002. There are therefore AERI profiles corresponding to nearly the entire period of MPL observations at SGP.

While the radiosonde and AERI data used in this study measure the same variable, the thermodynamic profiles from the two sources are not identical. When the AERI θ_v profiles are matched to radiosonde launch times and the radiosonde θ_v profiles are interpolated to match the AERI vertical resolution, there is strong but not perfect agreement between the two instruments. The linear regression returns an R^2 value of 0.86. Because the size of the data set renders a traditional scatterplot uninformative, Figure 2.2 uses a two-dimensional kernel density estimate instead to represent the probability density function; this method is further described in Chapter 6.

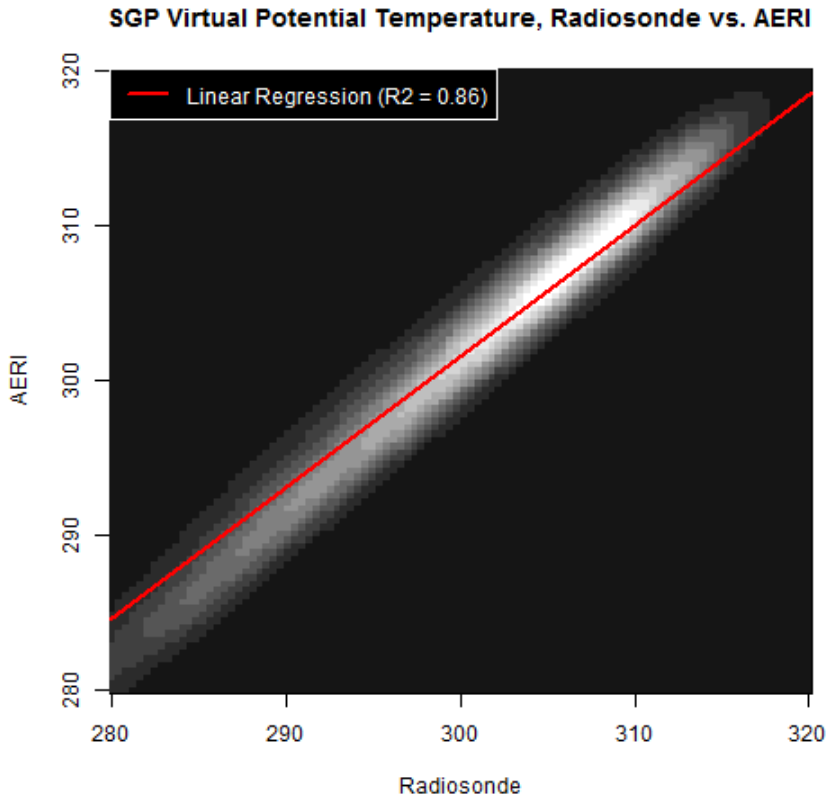

Figure 2.2. All θ_v values, irrespective of height, from radiosonde and AERI during the study period at SGP.

Systematic disagreement between the two instruments is small compared to the random variation, but θ_v values taken from the AERI instrument are almost 2 K warmer on average than θ_v values taken from radiosonde observations. For the lowest 3 km of the troposphere, where the PBL top is most likely to occur, the difference between the two instruments varies relatively little with height (Figure 2.3). Fortunately for this study, there is no indication that systematic error in either instrument would distort the appearance of inversion layers. Since the average difference between the radiosonde and AERI profiles remains nearly constant with height, the gradient in virtual potential temperature with height is the same for both instruments; the only exception is a small

persistent inversion in the mean radiosonde profile that does not occur in the mean AERI profile. Except for a narrow range below 500 m and in cases of random error, both instruments would measure the same strength for an inversion at the PBL top.

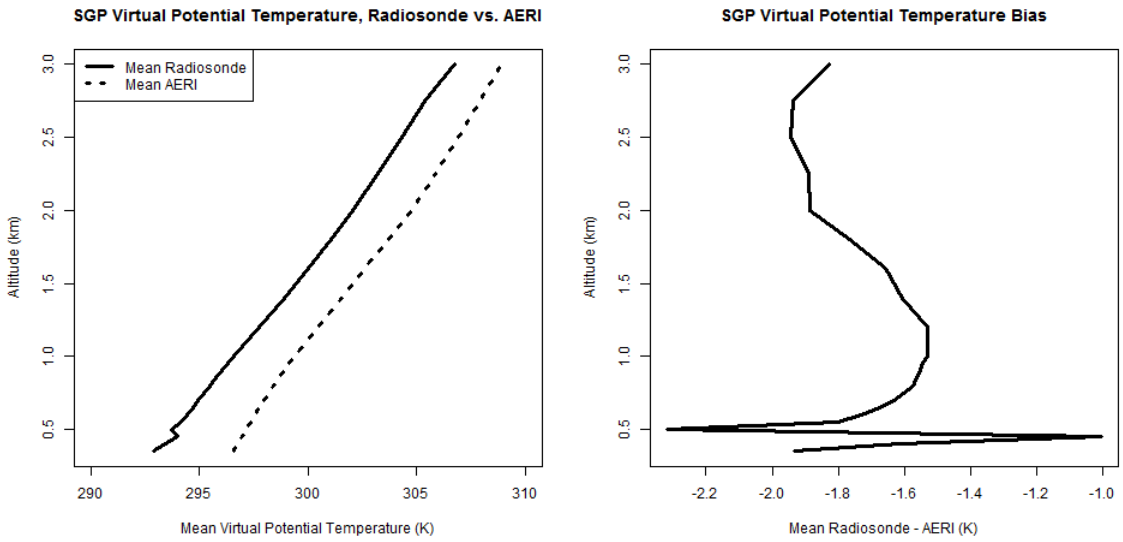

Figure 2.3. Mean θ_v profiles from radiosonde and AERI (left) and their mean difference with altitude (right).

2.3 Column Aerosol Optical Properties

While the aerosol backscatter detected by MPL is related to its optical depth, a separate instrument is needed to measure AOD and SSA in absolute terms. Unlike the atmospheric profile measurements described above, the AOD and SSA measurements used in this study are observed as column values integrated over the entire depth of the atmosphere.

For the SGP site, AOD and SSA measurements are taken from the Aerosol Best Estimate Value-Added Product, a data product of the US Department of Energy's ARM

program that takes advantage of the multi-instrument site at SGP. [*Flynn et al.*, 2012]. This data product combines AOD observations from three instruments—multifilter rotating shadowband radiometer (MFRSR), normal incidence multifilter radiometer (NIMFR), and shortwave array spectroradiometer – hemispheric (SASHE)—and other optical properties, including SSA, from the Aerosol Observing Station. It interpolates over gaps in order to produce a near-continuous record despite cloudy weather and instrument failures. Because the PBL has a strong diurnal cycle independently of aerosol conditions, and because the 500 nm wavelength is most directly comparable to the wavelengths used for MPL, the measurements used in this project are the daily mean values of 500-nm AOD and SSA (with observations taken during daylight only). Daily mean 500-nm AOD and SSA values are likewise used for the HeRO site, which has been equipped with a PREDE sky radiometer since March 2007 [*Wang et al.* 2014]. Crucially for the project, the HeRO site has very different aerosol conditions from the SGP site, with an AOD range more than four times greater and SSA measurements with a correspondingly more reliable precision (Figure 2.4).

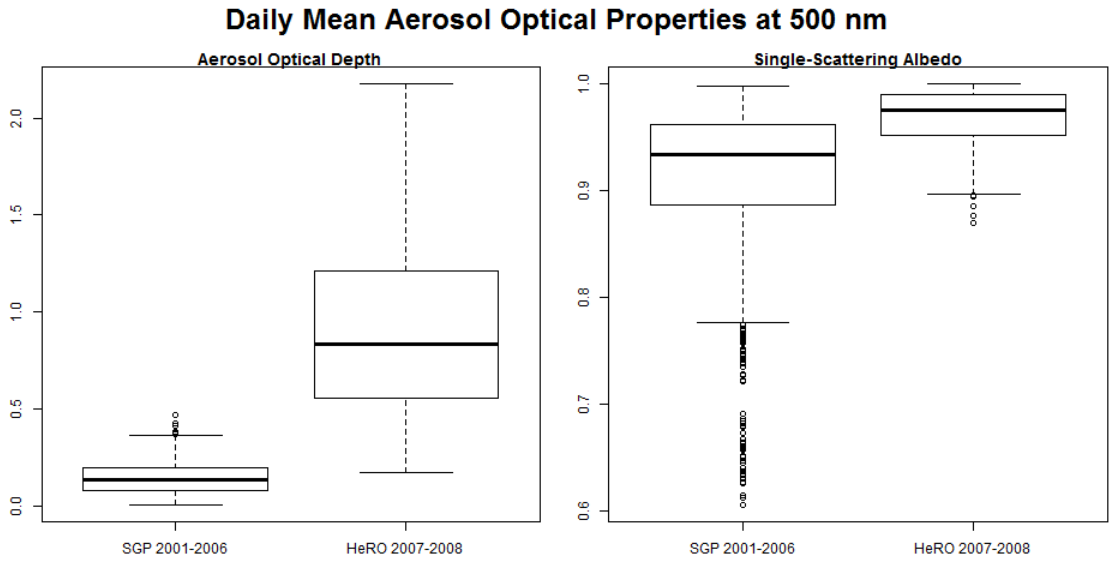

Figure 2.4. Range of AOD and SSA values at the SGP and HeRO sites.

2.4 Model Output and Previous PBL Results

The comparison between observations is more meaningful if accompanied by a theoretical framework. To complement the observations, Dr. Shuyan Liu constructed a WRF-Chem model simulation for a month-long span within the period of MPL observations at SGP. WRF-Chem operates on a regional scale with resolution high enough to simulate mesoscale processes. It also has a number of options for built-in PBL calculation, though all of them are based on the turbulent definition of the PBL. Turbulent mixing is more difficult to observe in nature than the thermodynamic properties that form the basis of MPL-based PBL detection, and it is not always clear that the two PBL definitions describe the same physical feature [*Seibert et al.*, 2000].

The built-in PBL schemes each use one of two main methods. The simpler of the two is the bulk Richardson number method [*Seibert et al.*, 2000; *Georgoulias et al.*,

2009], which is suitable whether the boundary-layer turbulence is primarily due to convection or wind shear. The bulk Richardson number is defined

$$R_B = \frac{g\Delta\overline{\theta}_v \Delta z}{\overline{\theta}_v[(\Delta\overline{U})^2+(\Delta\overline{V})^2]}, \qquad (2.1)$$

where θ_v is again the virtual potential temperature, U and V are horizontal winds, and g is gravitational acceleration; bars indicate mean values. It serves as a measure of the turbulence of the air for a height interval Δz. The PBL is then defined as the lowest height at which R_B exceeds the critical value 0.25 [*Hennemuth and Lammert*, 2006]. Other schemes rely on turbulent kinetic energy (TKE), which is defined

$$\frac{TKE}{m} = \frac{1}{2}\left(\overline{u'^2} + \overline{v'^2} + \overline{w'^2}\right). \qquad (2.2)$$

Here *u'*, *v'* and *w'* represent the turbulent component of the mean wind in each vector direction. The conceptual model of the PBL considers TKE to be uniform with height within a well-mixed boundary layer, then rapidly decreasing at the transition to the free troposphere [*Stull*, 1988]; this is the same basic structure that appears in the aerosol backscatter signal. However, neither the bulk Richardson number method nor the various TKE approaches respond directly to changes in mixed-layer radiative forcing. *Hu et al.* [2010] found that the Yonsei University (YSU) scheme, which had recently been updated, and the new asymmetric convective model, version 2 (ACM2) scheme, outperformed other commonly-used PBL schemes. Considerable uncertainty nevertheless remains in model PBL schemes, and it is necessary to keep several versions available to

modelers. Dr. Liu's simulation used YSU, a PBL scheme based on the bulk Richardson number method, to calculate PBL depths for the purposes of comparison to observations.

The period at SGP chosen for simulation was April 2004. This month was chosen for its high contrasts in daily mean AOD values, which varied between 0.1 and 0.4, sometimes dramatically from one day to the next (Figure 2.5). SSA values remained close to 0.9 throughout the month, as is most often the case for the site as a whole. In addition to reducing the computational requirements of the model run, the choice of a single month with varied AOD eliminates seasonal differences from the simulation.

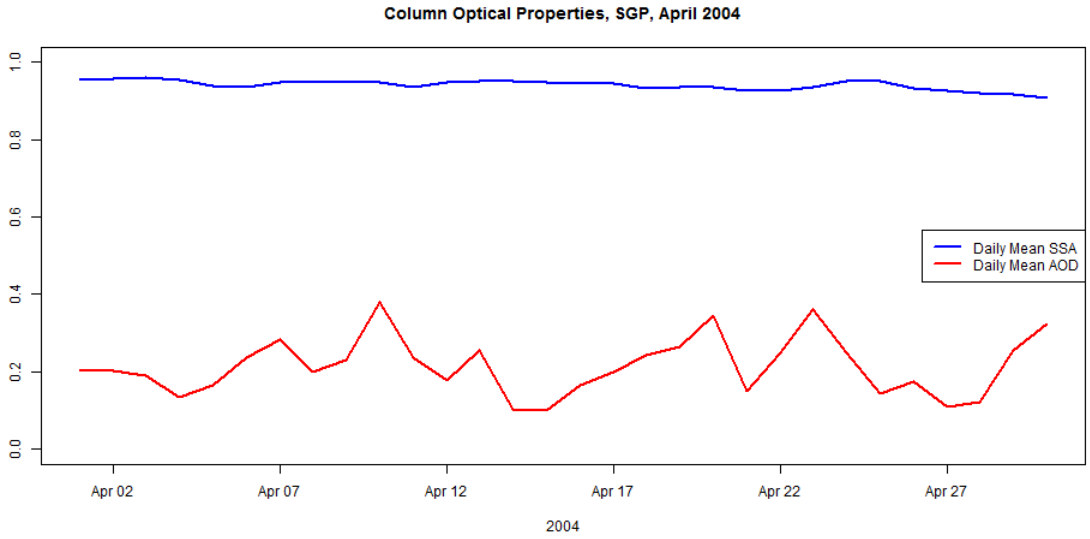

Figure 2.5. Daily mean AOD and SSA at the SGP site for April 2004, observed during the period of the WRF-Chem simulation.

Finally, this study uses PBL depth results provided by Dr. Shuyan Liu and described in *Liu and Liang* [2010], resulting from radiosonde observations at SGP. The PBL detection algorithm used in that study first evaluates to which of three regimes the potential temperature profile belongs: unstable, neutral or stable. The surface type (land,

ocean or ice) must be known in order to correctly diagnose the profile. The stability of the profile then determines the method used to find the height of the inversion (Figure 2.6). For unstable and neutral regimes, the CBL is defined as the level at which an air parcel rising from the surface would become buoyantly neutral. For stable regimes, the SBL must be determined based on whether it is driven by buoyancy or by shear from a nocturnal low-level jet (LLJ); it may be shallower than the top of the stable layer if the LLJ nose is within that layer. These PBL results generally correspond well to the YSU scheme from WRF-Chem and show realistic diurnal and seasonal cycles over the long term at SGP. They are a useful basis of comparison for the various other sources of PBL depths discussed in this project.

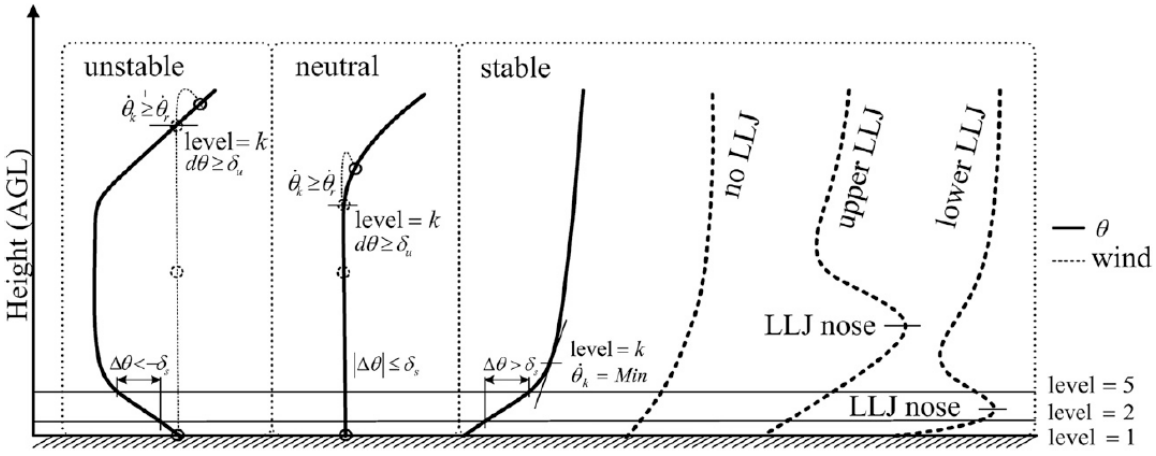

Figure 2.6. From *Liu and Liang* [2010], θ_v profiles representing idealized PBL regimes and PBL depth determination procedure.

Chapter 3. PBL Detection

3.1 Backscatter Gradient Methods

While it is possible to detect the PBL using the variance in lidar backscatter [*Jordan et al.*, 2010; *Kong and Yi*, 2015], backscatter gradient methods are more common and have used a number of approaches. The simplest ways to detect the PBL using aerosol backscatter gradient are to define a threshold value for the transition from mixed layer to free troposphere [*Melfi et al.*, 1985; *Palm et al.*, 1998] or to find the maximum of the first derivative of the backscatter signal [*Amiridis et al.*, 2007; *Tskaknakis et al.*, 2011]. With the backscatter signal formatted as an image file, it is also possible to detect layers by using edge detection software in programs such as Photoshop [*Parikh and Parikh*, 2002]. All these methods are effective for short-term, relatively uniform data sets, but they require either too much prior knowledge about the instrument and atmospheric conditions, or too much human judgment, to automate over multiyear data sets or multiple sites.

By contrast, the wavelet covariance transform method [*Davis et al.*, 2000; *Brooks*, 2003] is commonly used for longer time series because it can adapt to very different backscatter signals without additional human input. It compares the backscatter sounding to the Haar wavelet, defined as

$$\left(\frac{z-b}{a}\right) = \begin{cases} -1: & b - \frac{a}{2} \le z \le b \\ 1: & b \le z \le b + \frac{a}{2} \\ 0: & elsewhere \end{cases}, \qquad (3.1)$$

where a is the dilation of the Haar wavelet, b is the translation of the Haar wavelet, and z is the altitude. The wavelet covariance transform, $W_f(a,b)$, is expressed as

$$W_f(a,b) = a^{-1} \int_{zb}^{zt} f(z) h\left(\frac{z-b}{a}\right) dz \,, \qquad (3.2)$$

where *f(z)* is the backscatter sounding. The maximum value of $W_f(a,b)$ occurs where b equals the altitude of the strongest negative gradient in the backscatter; this is the top of the PBL. In equations 3.1 and 3.2, the dilation a corresponds physically to the depth of the transition zone between the mixed layer and the free troposphere. The given PBL depth is the center point in this zone, midway through the capping inversion or layer of entrainment.

The algorithm can be repeated while varying a to find its optimal value, representing the entrainment zone depth (EZD). Figure 3.1 shows the PBL depths resulting from a single lidar backscatter profile (21:00 UTC Aug. 15, 2003, at the SGP site) at many values of a. The chosen profile is typical in that for very small values of a the algorithm detects noisy PBL depths because of spurious gradients; for very large values, the detected PBL is too high. In the middle, however, is a wide range of a values for which the algorithm plateaus at the correct PBL depth. The entrainment zone depth (EZD) is the smallest value of a capable of finding the plateau PBL depth [*Brooks*, 2003]. For the profile in the figure the EZD is 400 m deep. However, a constant dilation value can be used as long as it falls within the plateau range for most profiles; this greatly reduces the computational requirements. In this project, a is held constant at 1 km.

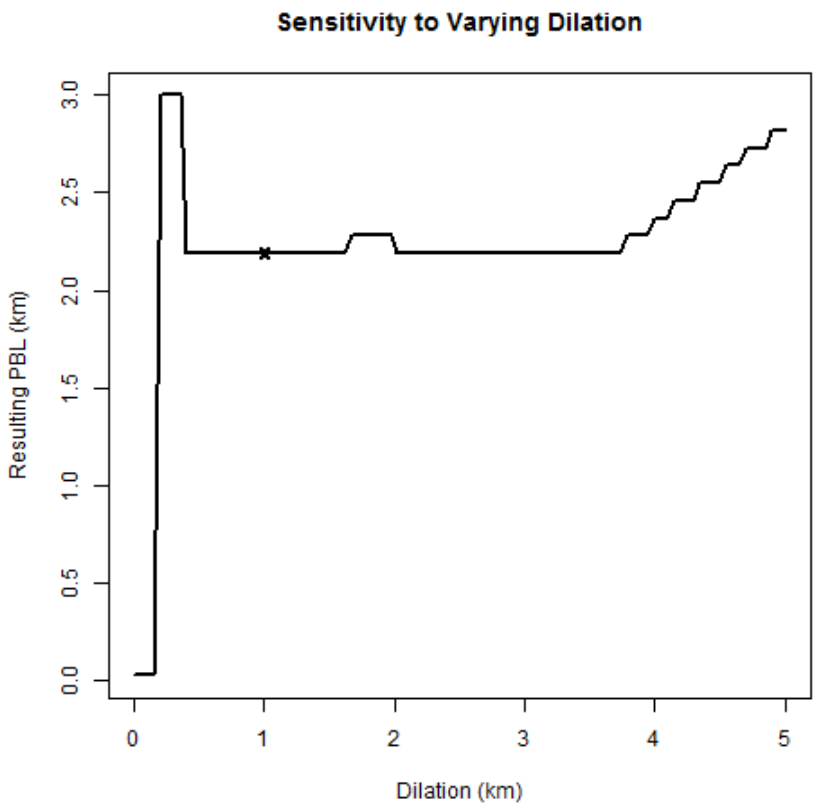

Figure 3.1. Wavelet covariance-detected PBL depths with varying dilation. The assumed 1-km dilation (crossed) is within the plateau range.

The wavelet covariance transform requires less prior information about the atmosphere or the lidar than many other PBL detection algorithms, and works equally well with data from several instrument types. This makes the algorithm useful for automated PBL detection in multiple data sets. It is independent of absolute backscatter values as long as the signal-to-noise ratio is high enough to distinguish the PBL. However, strong backscatter signals from high clouds and elevated aerosol plumes often overshadow the signal from the PBL, causing an elevated bias in PBL detection. *Lewis et al.* [2013] uses image processing methods to correct the wavelet covariance transform

algorithm in such cases. However, the solution used in this study is to limit the vertical extent of the backscatter profile to which the algorithm is applied. While the full vertical profile for lidar backscatter extends tens of kilometers into the atmosphere, the PBL does not occur beyond the low troposphere; a limit on the algorithm of 3 km is suitable for temperate sites such as in the US and China. This also reduces the computing time.

Steyn et al. [1999] developed a different algorithm for PBL detection in the lidar backscatter gradient. To avoid the problems posed by multiple non-PBL features in the backscatter, the algorithm uses the shape of a curve representing an idealized backscatter profile, namely,

$$B(z) = \frac{(B_m + B_u)}{2} - \frac{(B_m - B_u)}{2} \operatorname{erf}\left(\frac{z - z_m}{s}\right). \qquad (3.3)$$

Here, B_m and B_u are the backscatter values for the mixed layer and the lower free troposphere, respectively, z_m is the depth of the PBL, and s is a parameter defining the depth of the sigmoid curve between B_m and B_u. As before, z_m is defined as the center of a transition zone, which in this case has a depth equal to 2.77 times the value of s, assuming as in *Steyn et al.* [1999] that the entrainment zone encompasses 95% of the depth of the curve. The algorithm solves for these four parameters simultaneously to minimize the root-mean-square difference between the idealized curve and the backscatter sounding. As such, it arrives at an estimate of the transition, or EZD, as well as the PBL depth. Simulated annealing, as detailed by *Press et al.* [1992], is a robust method for fitting the curve; the fit improves with the quality of the initial guess. *Steyn et al.* [1999] used the algorithm with airborne lidar data, which necessarily operates for

short periods of time alongside other instruments. For longer-term, ground-based deployments, no single initial guess is appropriate for the entire time series.

The simulated annealing routine escapes from local minima and troughs that would trap a downhill simplex routine because it introduces a small random element to the solution [*Press et al.*, 1992]. It can therefore find multiple solutions given the same input. Over a time series in which the PBL changes slowly compared to the measurement interval, PBL returns from a simulated annealing algorithm appear "noisy", with unrealistically abrupt changes in height. *Hägeli et al.* [2000] details the appropriate interval for a running-mean filter, based on the dimensions of the data and the estimated vertical motion at the boundary layer top. For a stationary lidar deployment, a 25-minute interval matches the scale of the boundary-layer turbulence. With smoothing, the *Steyn et al.* [1999] algorithm is more sensitive to small-scale boundary layer waves than the wavelet covariance transform. Because curve-fitting uses the whole backscatter signal as a single shape, it also tolerates more extraneous features and noise.

Ground-based MPL cannot retrieve backscatter near the surface. Regardless of algorithm, shallow PBLs are sometimes missed, and RLs are detected instead.

3.2 The Combined Algorithm

The advantages and disadvantages of the two gradient methods suggest that PBL depth detection might be improved by using both in combination. The wavelet covariance transform is suitable alone for automated PBL detection, but it can also generate a first guess for the simulated annealing routine. The backscatter values for the free troposphere

and the mixed layer are the mean backscatter values above and below the first-guess PBL, respectively, and the EZD is the 1 km assumed by the wavelet covariance transform. In turn, the curve-fitting process refines the PBL solution so that it is less sensitive to elevated cloud and aerosol layers and more sensitive to changes in the boundary layer depth, while simultaneously solving for the depth of the aerosol transition. The resulting two-step process remains simple enough for the computational limitations of long-term automated analysis. In Figure 3.2, the combined algorithm is demonstrated using a single backscatter profile taken 21:00 UTC Aug. 15, 2003 at the SGP site.

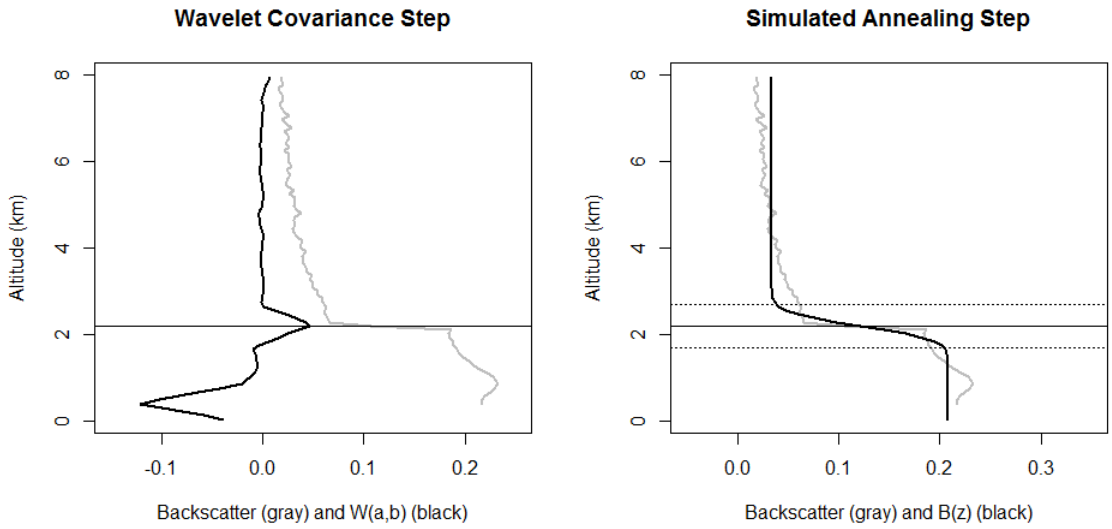

Figure 3.2. The combined PBL detection algorithm using an example MPL backscatter profile from SGP. The solid horizontal line is the PBL depth detected by each algorithm step. The dotted lines show the limits of the EZD.

The algorithm considers each backscatter profile separately until the final step, in which the running-mean filter suggested by *Hägeli et al.* [2000] is applied. Figure 3.3

illustrates how this smooths the PBL time series to eliminate random jumps introduced by the simulated annealing process. PBL depths for the MPL at SGP are detected at a 5-minute resolution, so the 25-minute smoothing interval is a five-cell filter. The details of small-scale waves within the boundary layer top are preserved in the final time series.

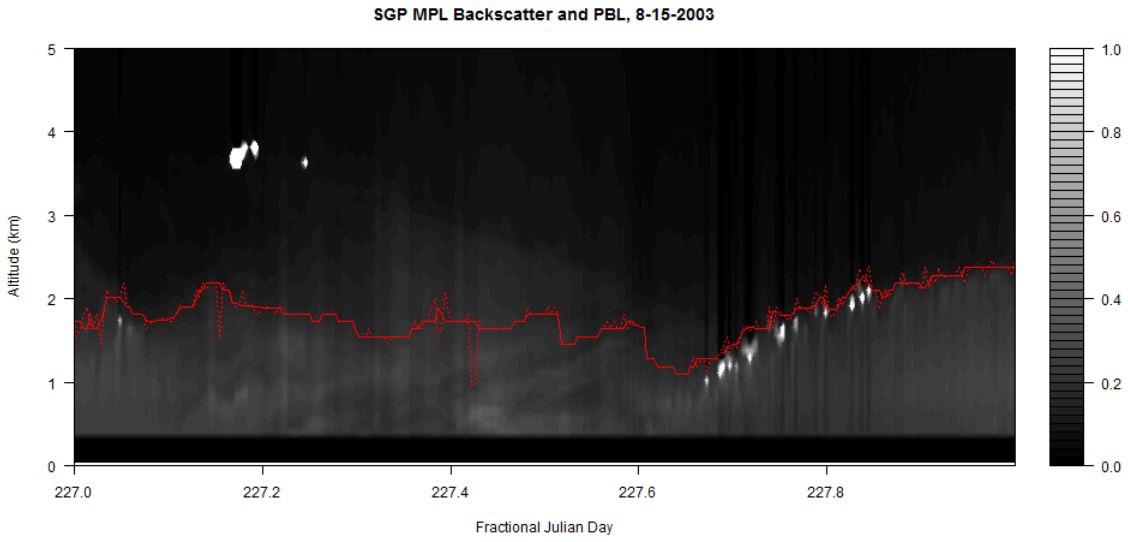

Figure 3.3. Aug. 15, 2003 at SGP. The dotted line indicates the PBL detected by the combined algorithm before smoothing; the solid line applies the running-median filter.

With modification, the same algorithm can be applied to thermodynamic profiles from radiosondes and ground-based remote sensing. For the AERI instrument at SGP, this is the first attempt to detect the PBL depth; for radiosonde, using the same algorithm as the other two instrument sources instead of the *Liu and Liang* [2010] results (for example) eliminates differences in algorithm bias as a variable in the comparison. Defining the PBL as before—the center of an inversion in the virtual potential temperature (θ_v) profile [*Stull*, 1988]—the algorithm must detect a sharp increase in θ_v

with height between the nearly-uniform mixed layer and the more stable free troposphere above. This means that the wavelet covariance part of the algorithm must use the negative of equation (3.1), that is

$$\left(\frac{z-b}{a}\right) = \begin{cases} 1: & b - \frac{a}{2} \le z \le b \\ -1: & b \le z \le b + \frac{a}{2} \\ 0: & elsewhere \end{cases} . \qquad (3.4)$$

Care must be taken to exclude the tropopause from analysis, but it seldom appears at altitudes where the PBL might be expected. In addition, the thermodynamic profile as a whole is often too stable for the algorithm to distinguish inversions. It performs more reliably if the linear regression of the lowest few kilometers is subtracted from the profile, so that the detection algorithm analyzes deviations from the mean lapse rate. Then the curve-fitting process can refine the first guess and estimate the EZD as before.

Chapter 4. Instrument Intercomparison at SGP

4.1 Intercomparison of PBL Depth Detection

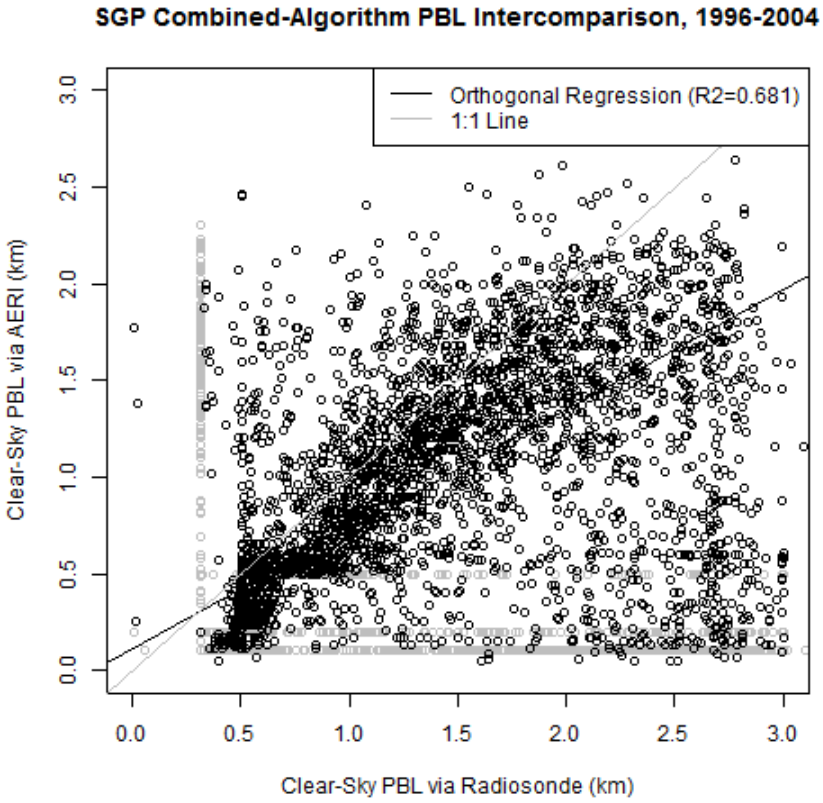

Figure 4.1. Comparison between AERI- and radiosonde-derived PBL depths at SGP. After the removal of artifacts indicating weak signal (gray points), the orthogonal regression is $PBL_{AERI} = 0.62 PBL_{sonde} + 0.12$.

The algorithm is evaluated by comparing PBL results from each instrument at SGP against one another. Because they are from the same site, their time series are matched to one another and the PBL depth detection uses the same algorithm, the comparison minimizes variables. In the case of AERI vs. radiosonde (Figure 4.1), the measurements are two sets of thermodynamic profiles; the differences in PBL depth come from differences in instrument precision and resolution. This is especially clear in

the very shallow PBL depths, as there are no radiosonde observations between the surface and approximately 300 m, while AERI has no such restriction. Because neither method is considered true, an orthogonal regression is used instead of a simple linear fit. Two-thirds of the variation is accounted for (R^2=0.681). Most points lie close to the 1:1 line. While the regression is influenced by a cluster of results in which the radiosonde-derived PBL depth is much higher than the AERI-derived PBL depth, the overall systematic error is low. Much of the correspondence with AERI data is only achieved using the combined algorithm, because the low vertical resolution of the AERI-derived thermodynamic profiles strongly affects the wavelet covariance transform.

For comparison between radiosonde and MPL-derived PBL depths, it is important to assure that clouds do not interfere with PBL detection (Figure 4.2). Clouds return strong backscatter at the lidar wavelength, and the attenuation of the laser pulse through an optically thick cloud deck appears as a sharp backscatter gradient that may be targeted by the PBL detection algorithm; the same features can be used to produce cloud base and top heights as a standard MPL data product [*Sivaraman and Comstock*, 2011]. The wavelet covariance transform component of the PBL detection algorithm is restricted to 3 km from the surface, partly because the PBL typically occurs there [*Stull*, 1988; see *Ma et al.*, 2011 for a rare exception], but partly to eliminate interference by higher-altitude clouds. However, most low-level cloud bases occur at or near the PBL, either because the capping inversion prevents stratocumulus clouds from developing farther or because the cloud base in a deep convective cell marks the PBL top [*Stull*, 1988]. The algorithm therefore returns an answer about as accurate as it would have from aerosol backscatter alone.

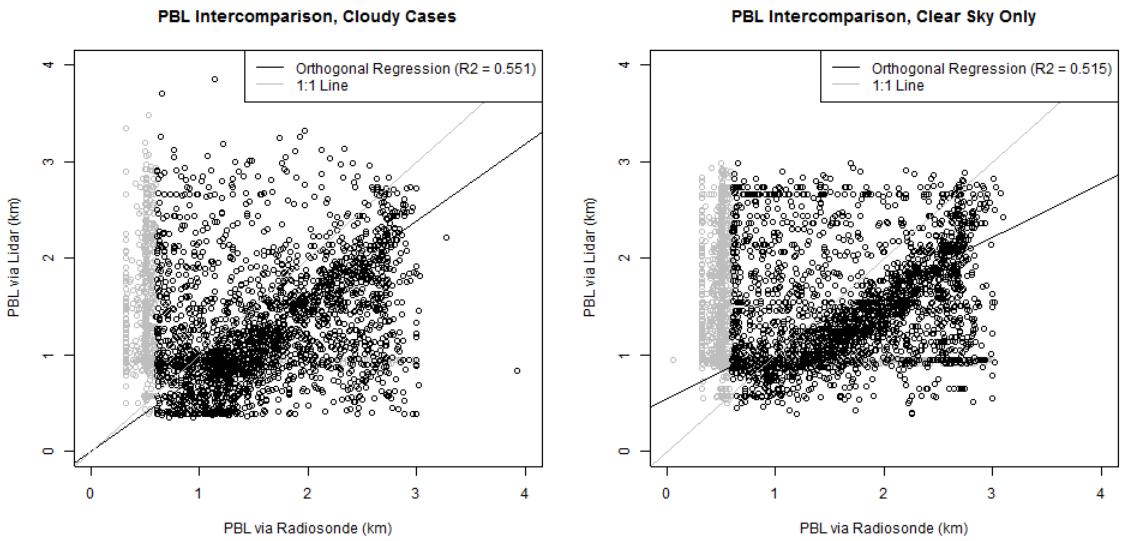

Figure 4.2. Radiosonde- vs. MPL-derived PBL depths at SGP, cloudy cases (left) and cloud-free cases (right). R^2 values for the orthogonal regression are 0.551 and 0.515, respectively. Gray points, excluded from regression, are outside the lidar overlap range.

In all MPL-derived PBL depths, the incomplete overlap between the laser beam spread and the telescope field of view imposes a lower limit on the instrument range. Radiosonde-derived PBL results below 600 m (27% of cases) are excluded from regression because the lidar cannot observe them, although radiosonde can. There is little difference between cloudy and cloud-free lidar PBL detection, however. The following intercomparison therefore uses the full set of results (Figure 4.3).

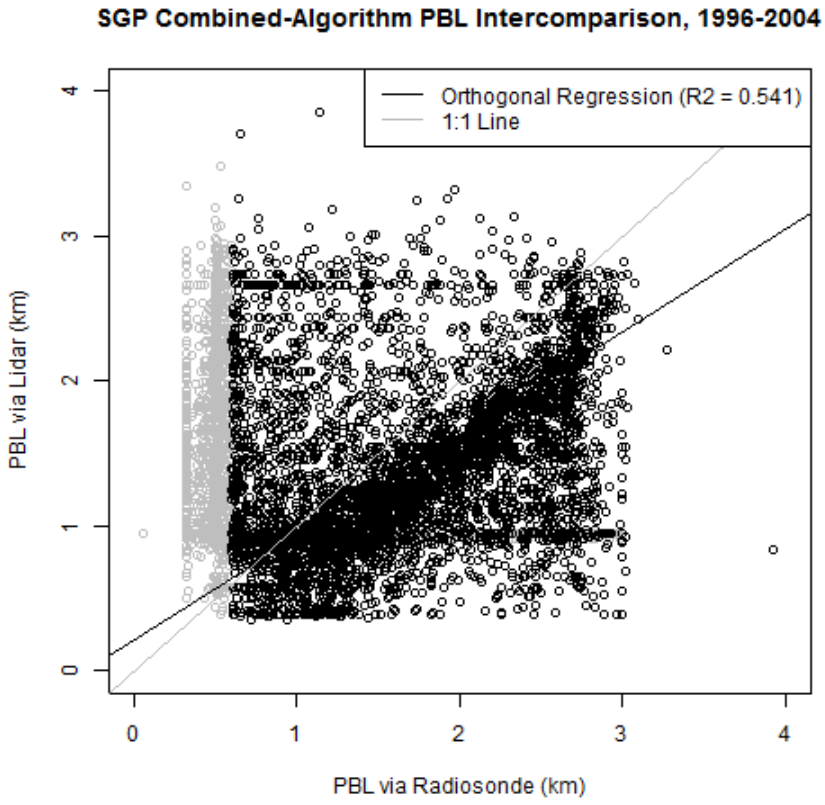

Figure 4.3. Intercomparison between all radiosonde- and MPL-derived PBL depths at SGP. The orthogonal regression is $PBL_{MPL} = 0.71 PBL_{sonde} + 0.22$. Gray points, excluded from regression, are outside the lidar overlap range.

4.2 Diurnal Cycles

Although the lidar-derived PBL depths are matched to radiosonde launch times, the comparison does not discriminate between day and nighttime observations. Continental boundary layers undergo strong diurnal cycling through regimes (Figure 4.4), classified according to whether the surface undergoes radiative heating (daytime) or cooling (night).

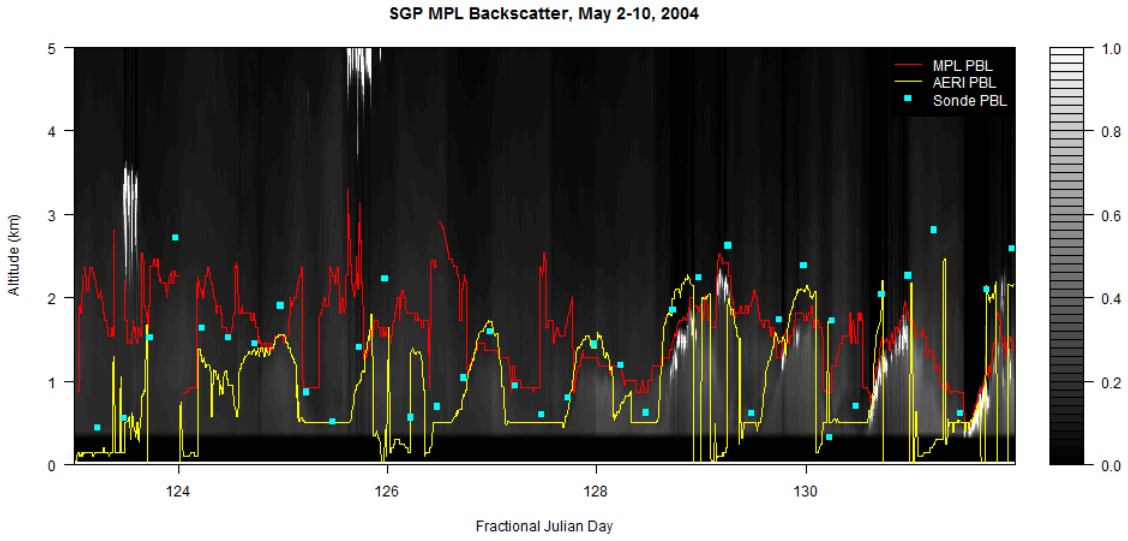

Figure 4.4. PBL heights detected by MPL, AERI and radiosonde, overlaid on MPL backscatter during a nine-day period of typical conditions.

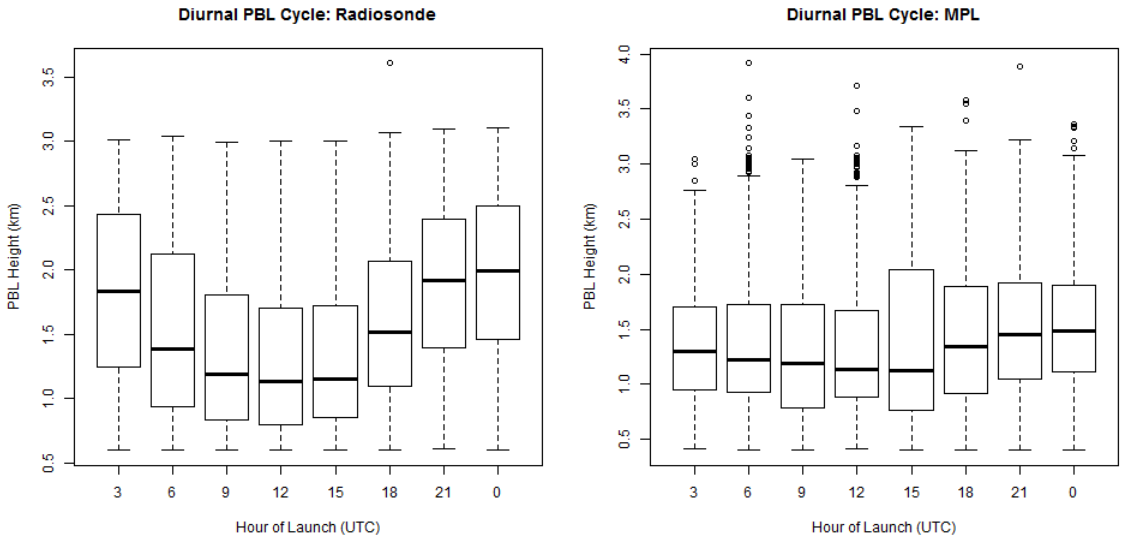

Figure 4.5. Boxplots show the distribution of PBL depths from different radiosonde launch times by radiosonde (left) and MPL (right), excluding PBL depths outside the lidar overlap range.

Figure 4.5 shows that as expected [e.g., *Stull* 1988] the PBL top depth as detected by radiosondes over the continental SGP site (results below 600 m excluded for comparison with MPL) has its minimum in the early morning and its maximum coinciding with peak convection in the afternoon. Lidar-derived PBL top heights show a cycle of the same phase, but smaller amplitude. The cosine curve fitted to the median radiosonde-derived PBL depth with time has an amplitude of 470 m and an R^2 value of 0.97. For MPL-derived PBL depths, the amplitude is only 170 m and the R^2 is 0.85. This may happen because the aerosol distribution through the column does not follow the thermodynamic profile exactly, especially during times of transition. In addition, some times of day allow for more accurate MPL-based PBL detection than others. This is especially true because nocturnal stable boundary layers are often shallow enough to fall below the lidar overlap range.

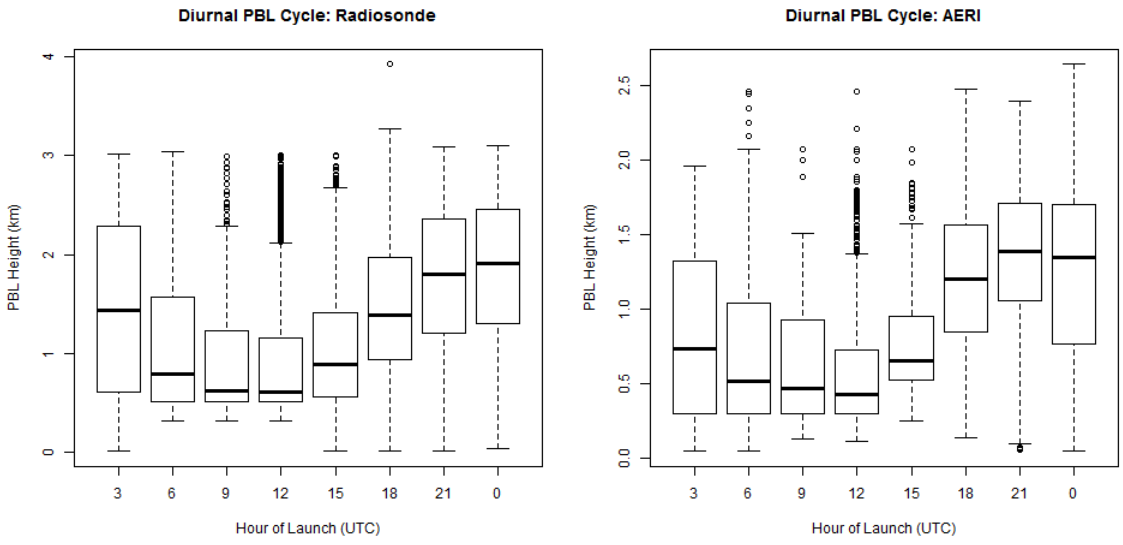

Figure 4.6. Diurnal variations of PBL depth from radiosonde (left) and AERI (right).

The AERI-derived PBL depths show a similar cycle (Figure 4.6) to the radiosonde-derived PBL, with shallow PBLs included in the analysis. While the MPL overlap range limits its ability to observe lower altitudes, the AERI profile improves near the surface. Because the vertical resolution of the instrument decreases with height, it can detect shallow PBL depths with greater precision than deeper PBLs. The results that can be compared to MPL-derived PBL depths, i.e. those that occur above the overlap range limit, are less reliable than the shallower AERI-derived PBL depths that can be compared only to radiosonde. Consequently, the relationship between AERI-derived and MPL-derived PBL depths is not strong enough for a meaningful comparison of the diurnal cycle. It makes more sense to compare the AERI-derived PBL diurnal cycle to that of radiosonde, this time with shallow PBL depths from both instruments included. The amplitude of the cosine regression expands to 660 m for radiosonde results ($R^2 = 0.90$). For AERI-derived PBL depths, the amplitude is 440 m and the R^2 value is 0.64. Because the strengths and limitations of the PBL products complement each other, all the products are valuable despite their inconsistency, with more or less reliability in different circumstances as detailed below.

The agreement of PBL detection by the three methods varies with the time of day as seen in Figure 4.7. Note that R^2 values do not fall between zero and one. To prevent any systematic error specific to one time interval from appearing as misleading high agreement, R^2 is always evaluated for the 1:1 line, i.e. perfect agreement between the two instruments, instead of the linear regression for each time interval. Daytime PBL top heights show closer agreement between instruments than nighttime PBL top heights, and mature boundary layers, whether stable or convective, show more agreement than

boundary layers that have just begun to collapse or develop. This may be partly because the radiosonde takes time to ascend, and the more snapshot-like profiles from MPL and AERI cannot match it exactly. Slowly changing PBL tops naturally make the best match. However, in the lidar, the same effect could also be due to pollutants that remain aloft in the RL when the convective boundary layer collapses, or that entrain downward into the growing convective boundary layer in the morning. Nocturnal stable boundary layers are more difficult to detect because the stability of that regime allows aerosols to form thin stratified layers instead of mixing uniformly. MPL-derived PBL depths show a greater influence of boundary layer maturity on the agreement with radiosonde than do AERI-derived PBL depths. This supports the idea that aerosols remain in the RL overnight, interfering with MPL backscatter gradient-based detection of the SBL, rather than matching the altitude change of the inversion in θ_v. The use of MPL backscatter gradient as a proxy for thermodynamic structure has some limitations that require other criteria to overcome, as suggested in *Lewis et al.* [2013].

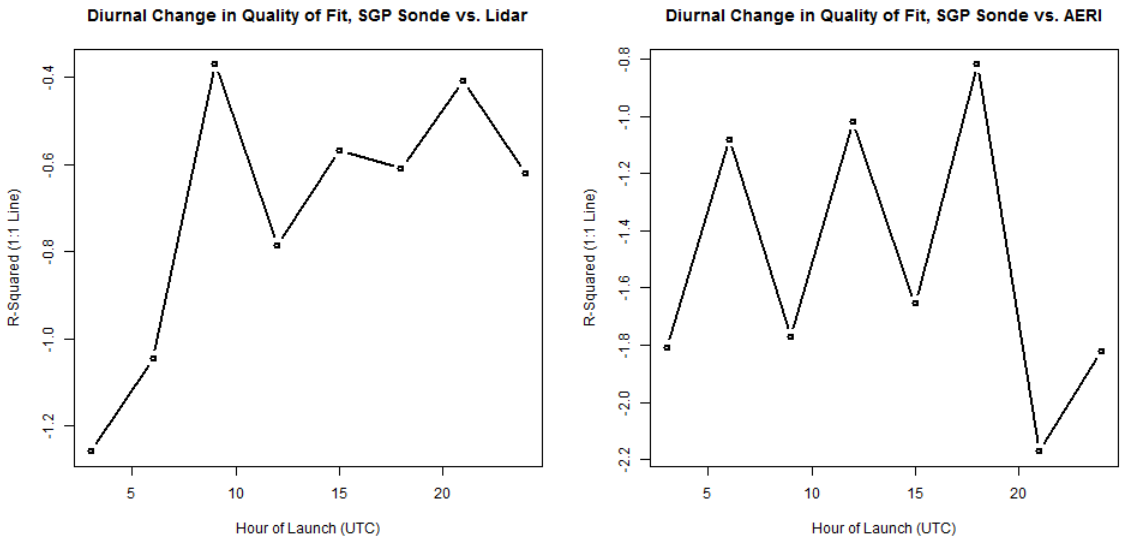

Figure 4.7. Variation of R^2 values with the time of radiosonde launches, assessing the quality of fit between PBL_{MPL} and PBL_{sonde} (left) and between PBL_{AERI} and PBL_{sonde} (right).

4.3 Seasonal Cycles

The seasonal cycle of the PBL depth is as important as the diurnal cycle to mixed layer processes. Surface convection is stronger in the summer months than in the winter at continental sites, and the PBL top depth responds accordingly. Again the radiosonde results follow a cosine curve, its peak coinciding with the most intense surface heating. The difference in wave amplitude between the radiosonde- and MPL-based PBL top heights is still present but less pronounced (Figure 4.8). The cosine curve fitted to the radiosonde-derived median values has an amplitude of 380 m and an R^2 value of 0.93, while the cosine curve fitted to the MPL-derived median values has an amplitude of 330 m and an R^2 value of 0.90. The radiosonde-derived PBL top heights average slightly higher and are more variable within any given month. This is consistent with the greater amplitude of the diurnal cycle shown in Figure 4.3.

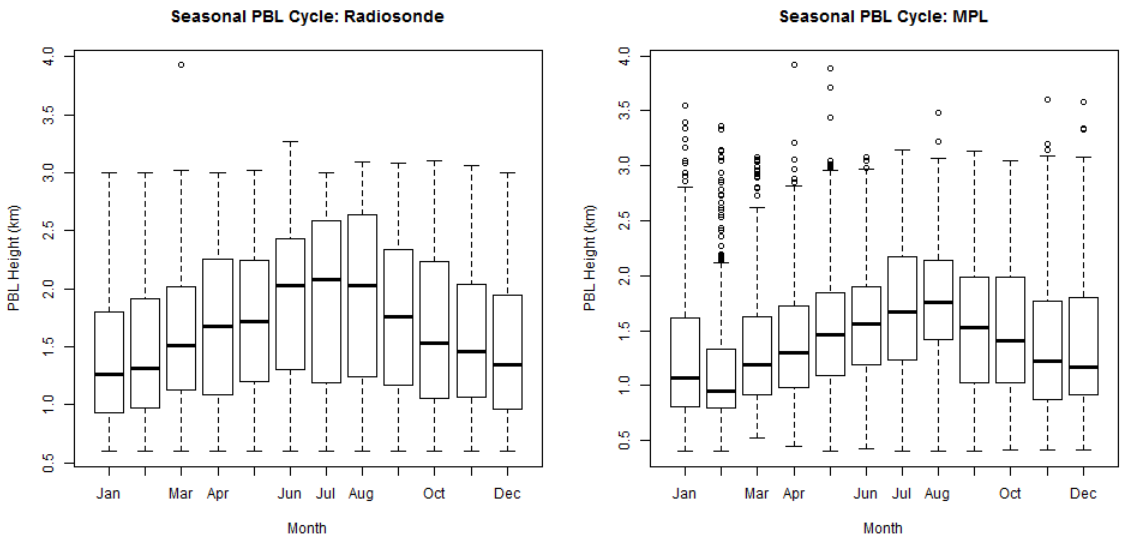

Figure 4.8. Boxplots show the distribution of radiosonde-derived and MPL-derived PBL depths by month, with shallow PBLs excluded from the radiosonde record.

It seems counterintuitive, given that convective PBLs are analyzed more accurately than stable nocturnal boundary layers, that the instruments diverge most in the summer months (Figure 4.9). For the diurnal cycle analysis, the highest PBL tops have the best agreement between the two instruments. For the seasonal cycle, they have the least, despite the fact that the MPL-derived seasonal cycle of PBL depths more closely resembles a cosine curve than the MPL-derived diurnal cycle. R-squared values vary to almost exactly the same degree as they do for the diurnal cycle shown in Figure 4.6, but this time there is a steep drop in the quality of fit in the summer and a peak in the winter months.

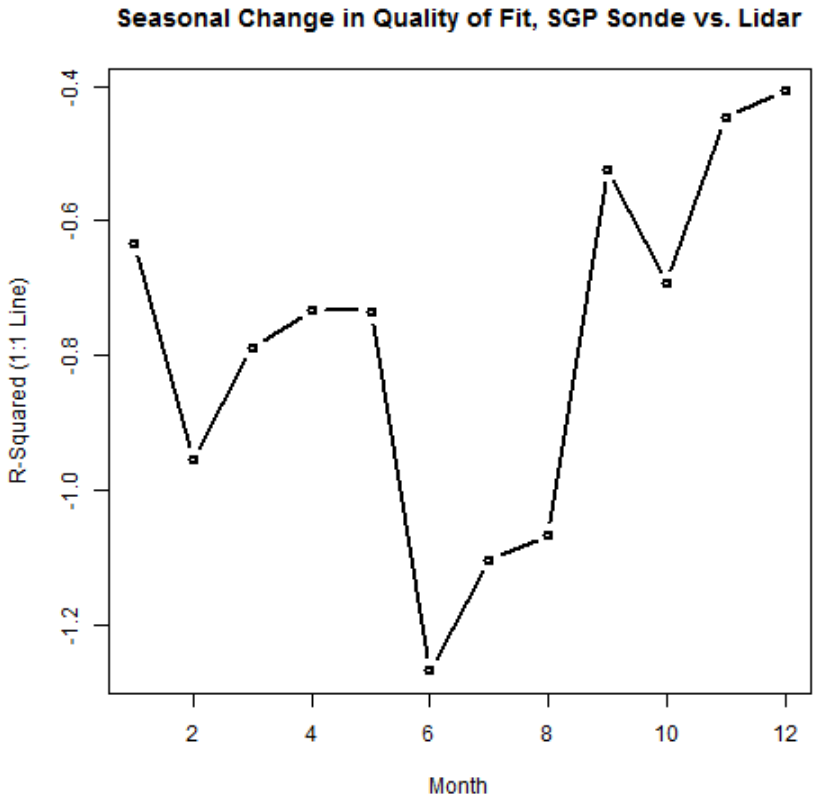

Figure 4.9. R^2 values assessing the quality of fit to the 1:1 line for the radiosonde-vs.-MPL intercomparison by month.

The difference between the seasonal cycles in Figure 4.8 appears mostly in the higher summertime PBL depths detected by radiosonde than by MPL, and this is a clue as to its cause. The reason for the discrepancy appears to be the effect of deep convection on the thermodynamic structure of the middle troposphere. Figure 4.10 shows the seasonal variation of MPL-retrieved cloud base heights occuring at altitudes below 4 km, which can be considered typical of boundary-layer clouds.

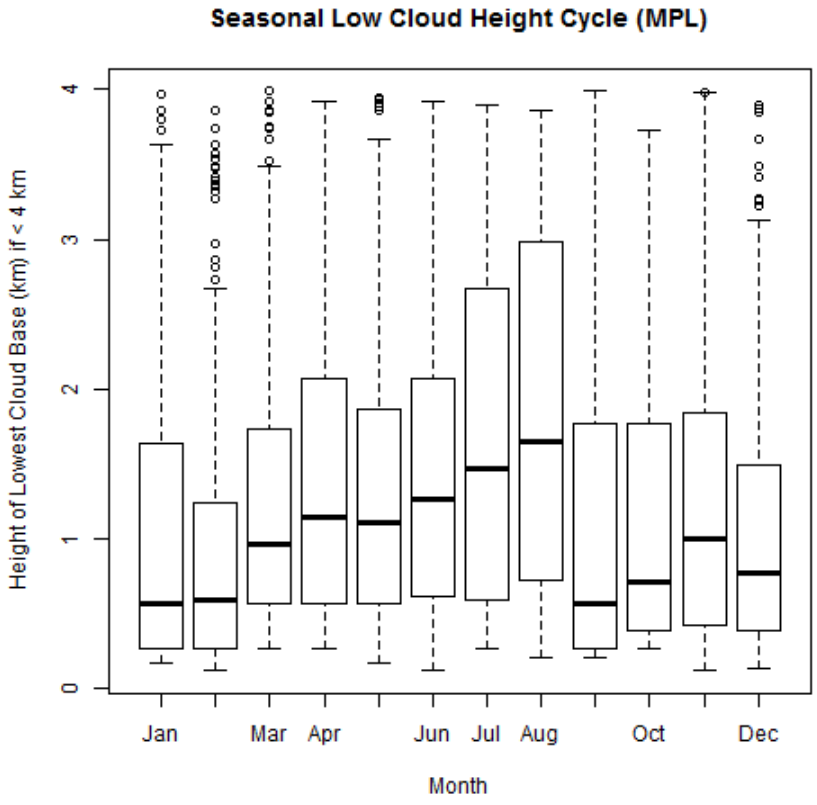

Figure 4.10. Boxplots show the monthly distribution of MPL-retrieved cloud base depths located below 4 km at the SGP site for the period 1996-2004.

The seasonal cycle peaks with a median cloud base height of approximately 1500 m in August, similar to the seasonal peak for the MPL-derived PBL depths. The radiosonde-derived PBL depths for the summer months are typically higher, and vary more. Although a schematic of PBL regimes in *Medeiros et al.* [2005] puts the PBL near the cloud base in cases of deep convection, the convective turbulence fueled by surface heating extends all the way to the cloud top, which may well reach the tropopause during the kind of deep convection that is typical of summer in the Southern Great Plains. Temperature and moisture properties are similarly carried upward into the cloud. This renders the thermodynamic definition of the PBL ambiguous (the algorithm is designed

with an altitude limit to avoid confusing the tropopause with the PBL) and in such cases, the MPL may be more accurate than radiosondes as a PBL detection tool.

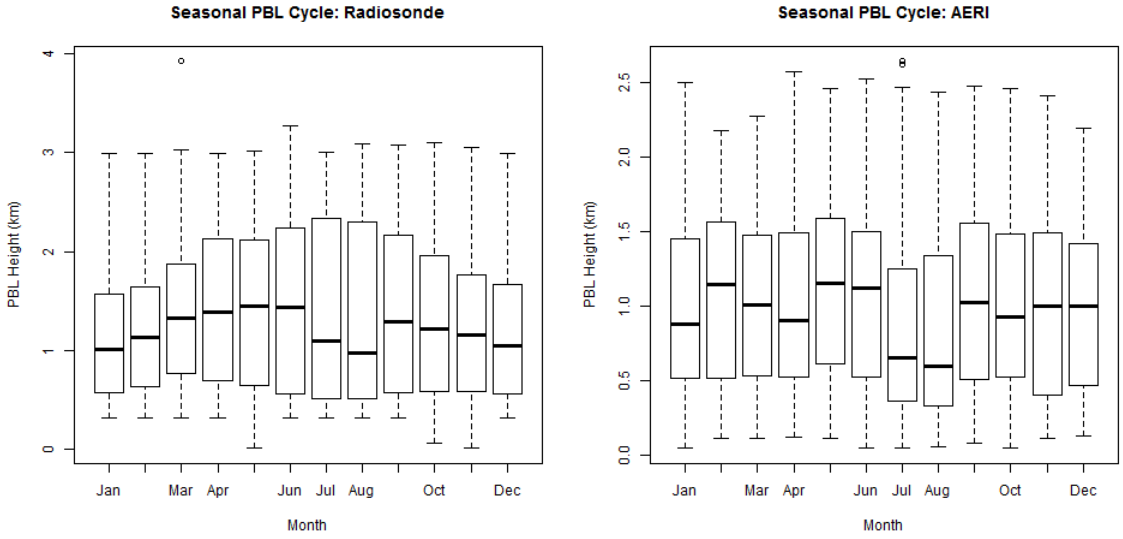

Figure 4.11. Boxplots for the monthly distribution of PBL depths from radiosonde and AERI, with shallow PBLs included.

Because the θ_v profiles from AERI and radiosonde have no overlap limitations, the comparison between AERI-derived and radiosonde-derived PBL depths is made without removing shallow PBLs (Figure 4.11). Both radiosonde and AERI show a high frequency of shallow PBL depths in July and August, which makes it impossible to fit a cosine curve to the seasonal variation. The AERI-derived and radiosonde-derived PBL seasonal cycles show a few similarities to one another: their PBL depths peak in May and June and trough in December and January. However, the radiosonde-derived PBL depths average higher in altitude than the AERI-derived PBL depths. The cluster of noncorresponding points in Figure 4.1 affects the overall seasonal cycle. As with the MPL results, the agreement between AERI and radiosonde drops in the summer months

(Figure 4.12). Again, this is because the radiosonde-derived PBL depths are higher; the AERI-derived PBL depths for July and August have medians well below the MPL overlap limits, and vary less. This is in error, since unbroken stretches of low-level temperature inversions are associated with cold weather rather than the convective Great Plains summer. However, because the AERI instrument has denser vertical resolution at lower altitudes, ambiguous thermodynamic profiles—as in deep convection—may result in lower average PBL depths from AERI.

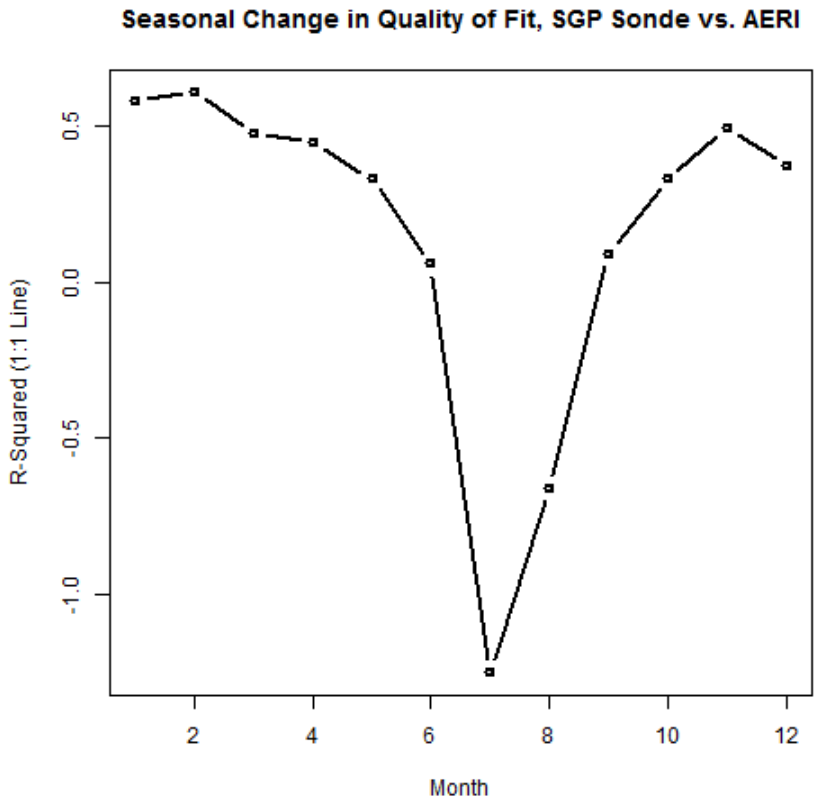

Figure 4.12. R^2 values assessing the quality of fit to the 1:1 line for radiosonde vs. AERI, shallow PBL depths included.

The agreement between MPL and radiosonde in the presence of boundary-layer clouds (Figure 4.2) conforms to expectations about boundary-layer stratocumulus, for which the cloud thickness remains shallow due to the PBL top acting as a capping inversion. This is one of several boundary-layer regimes discussed in *Medeiros et al.* [2005], which also notes two complications. The first is decoupling of the flow within the stratocumulus deck from the rest of the mixed layer. Decoupling does not imply an additional temperature inversion, but is mostly apparent in measurements capable of profiling vertical motion, including wind lidar. Decoupling within a cloud layer does not appear in thermodynamic profiles, and to lidar it is hidden by the opacity of the cloud. The second complication is the possibility of a low stable boundary layer forming well below the level of the lowest cloud base. The wavelet covariance transform may then miss the signal of the PBL top because of the much stronger gradient caused by cloud attenuation. The combined algorithm avoids this problem by restricting the depth of the profile used in analysis, but may still err if the PBL is shallow and the elevated cloud base occurs at an altitude reasonable for PBL depths. Lastly, lidar cannot distinguish between shallow stratocumulus and deep cumulus convection, although both are distinct from other cloud types. The PBL is detected where the backscatter signal fully attenuates, which is slightly too high for deep convection and slightly too low for a capping inversion over stratocumulus.

Steyn et al. [1999] recommends the simulated annealing routine partly because it finds the EZD, used to estimate fluxes through the boundary layer top. However, in the SGP results the detected EZD values hardly deviate from the constant initial guess, making EZD intercomparison among the different instruments impossible. A varying

initial guess for the EZD, as there is for the PBL, would produce better results. However, wavelet covariance-based determination of the EZD is only possible by trial-and-error repetition with different values of the wavelet dilation, a computationally intensive process. The transition between mixed-layer aerosol loading and the cleaner free troposphere may also have a different depth than the potential temperature inversion; aerosol content need not be as good a proxy for the transition as it is for the PBL. If this were the only obstacle, however, some relationship between radiosonde- and AERI-derived EZD results would be expected. None is found. EZD obtained by the combined algorithm is therefore unreliable, not suited to flux estimates.

For PBL detection, however, the benefit of the simulated annealing step is clear. Much of the correspondence in the AERI-derived PBL depth set is due to the use of the combined algorithm. Because the wavelet covariance transform works its way along the profile, comparing each data point to the others separately, the PBL depths it detects must fall on the same intervals as the original data; a low-resolution profile returns blocky, low-resolution PBLs. By contrast, the curve-fitting routine detects PBL depths based on the overall shape of the profile and is therefore free to return heights between the profile's data points. For intercomparison between instruments, this property eliminates aliasing caused by the differing height intervals of the profiling data. For PBL depths from a single instrument with high temporal resolution, it returns PBL depths with realistic rates of change and development that better match the shape of the contour in lidar backscatter or virtual potential temperature.

Chapter 5. Comparison Between MPL Sites

5.1 Diurnal Cycles

Once satisfied that the MPL-derived PBL depths are comparable to those obtained from thermodynamic profiles, it is possible to compare MPL results from SGP to PBL depths from MPL deployments at other sites. While radiosonde measurements are taken across widespread networks for weather forecasting purposes, potentially yielding PBL depth observations over large areas of land, typical sites make a radiosonde launch only twice per day.

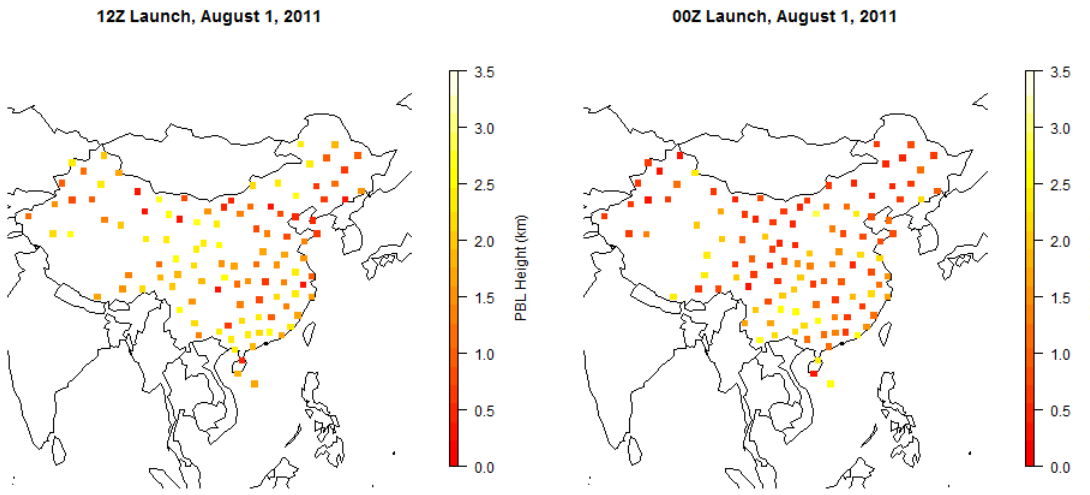

Figure 5.1. PBL depths analyzed for the operational radiosonde network in China, August 1, 2011.

Figure 5.1 illustrates the disadvantages of using the operational radiosonde network for PBL analysis: while the geographic coverage is extensive, the PBL depth varies spatially for too many reasons to draw conclusions about its patterns. More importantly, the diurnal variability of the PBL depth is hardly represented; there are only two data points,

and the timing of the launches is coordinated globally rather than targeted to the likely maximum and minimum PBL depth. In China, where the local time is eight hours ahead of universal coordinated time, the 00:00 UTC and 12:00 UTC launch times (i.e., 8:00 AM and 8:00 PM local time, respectively) are most likely to catch the PBL during a period of regime transition; in North America, where the time zone at the SGP site corresponds to UTC-6 (00:00 and 12:00 UTC correspond to 6:00 PM and 6:00 AM CST), operational radiosonde launches are made at nearly the worst possible time to observe mature SBL and CBL regimes. As a result, while the PBL depth record derived from the operational radiosonde network does show systematic differences between the two launch times—the 12:00 UTC launch, which takes place during or just after the CBL collapse in the evening, is consistently associated with deeper PBLs than the midmorning 00:00 UTC launch—it greatly underestimates the diurnal variability of the PBL depth and conveys almost no information about the structure of the diurnal cycle.

None of the MPL sites in China used in this study include intensive radiosonde observations like the frequent launches at SGP. However, with the MPL observations no longer bound to radiosonde launch times for the purposes of evaluation, this part of the analysis can use the full MPL temporal resolution. The mean diurnal cycle is therefore observable in much greater detail, though the accuracy varies by time of day as described in Chapter 4, and the overnight segment of the cycle in particular is skewed toward deeper residual layers. At three-hour intervals, the diurnal cycle fits a smooth cosine curve, but this obscures the rapid development of the typical CBL and the much slower change in the overnight SBL or RL. Furthermore, the diurnal cycle varies by season (Figure 5.2).

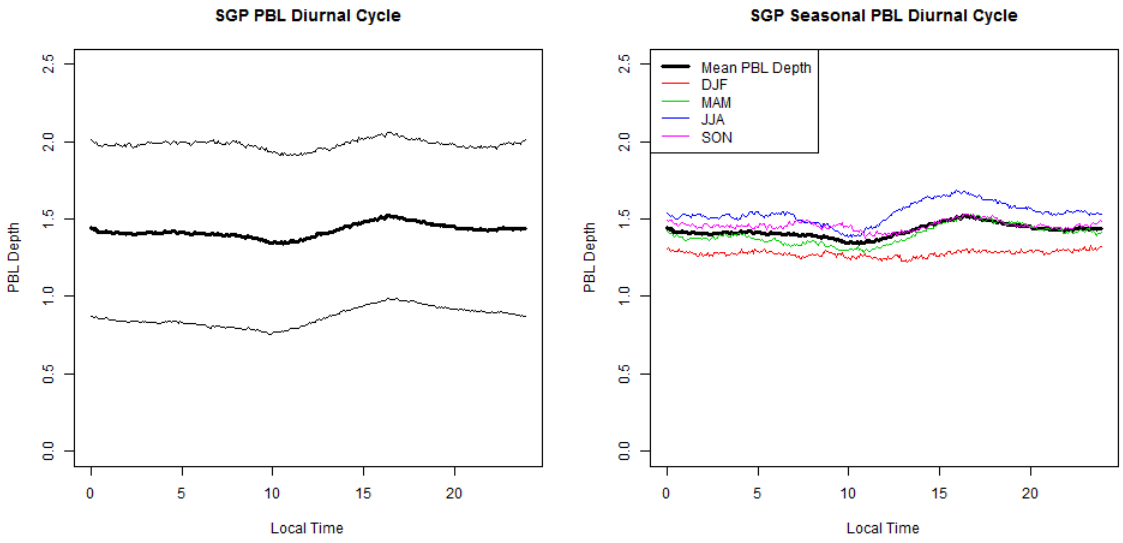

Figure 5.2. For SGP, the mean diurnal cycle of PBL depths at 5-minute resolution. Time of day is given in hours local time (UTC-6). Left, the overall mean and standard deviation; right, the overall mean and the mean for each season.

Because SGP is a continental site, the amplitude of the diurnal cycle is driven by surface convection: the deepest CBLs occur in summer, when surface convection is strongest, while the winter PBL stays shallower throughout the 24 hours and has no visible CBL development. There is little difference between the spring and autumn months, which show roughly equivalent transitions between winter and summer conditions. None of this is surprising given the *Stull* [1988] conceptual model. The only difference from expectations is the depth of the SBL, which is much shallower in most conceptual models. This is due to the tendency of MPL-based observations to miss shallow SBLs, especially but not exclusively those within the overlap zone, and mark the capping inversion, or top of the RL, as the PBL instead. The relatively deep overnight PBL explains why the diurnal cycle has a smaller amplitude than might be expected; it

also introduces an apparent delay to CBL development, since this is only visible starting from the point in midmorning that the CBL overtakes the RL. This tendency is equally true for all MPL deployments using this PBL detection algorithm, however; the overnight PBL depths follow the same pattern at the HeRO site (Figure 5.3) and at Xianghe and Shouxian (Figure 5.4). Because all four sets of PBL results have this effect in common, it does not affect the comparison among MPL-based PBL depths from the same detection algorithm but different sites.

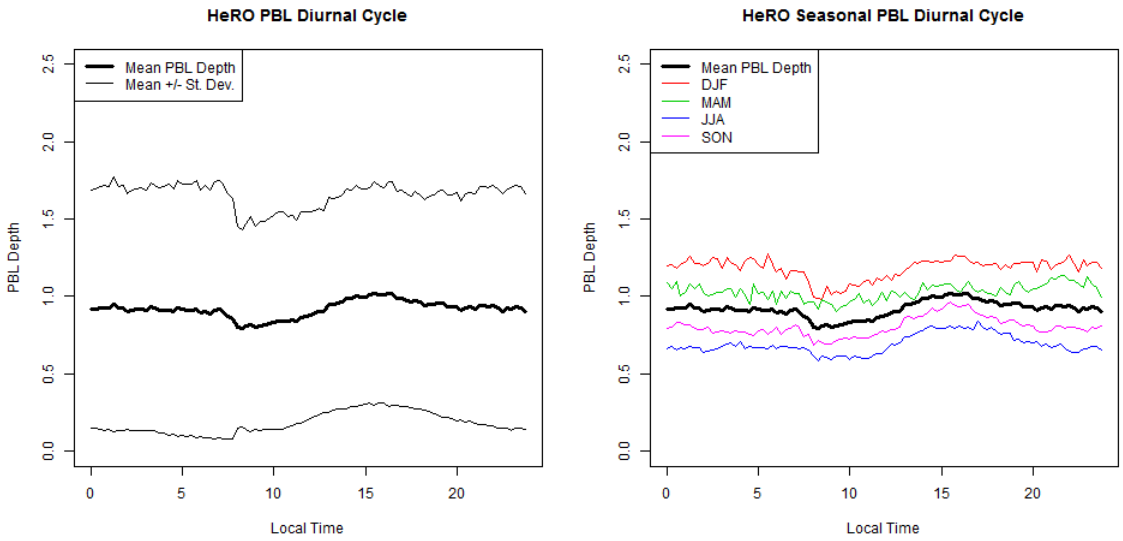

Figure 5.3. The same as Figure 5.1 but for Hefei, where the temporal resolution is 15 minutes. Time of day is given in hours local time (UTC+8).

At the HeRO site, the temporal resolution is 15 minutes instead of the 5-minute intervals available at the other sites, and the smoothing interval recommended by *Hägeli et al.* [2000] is omitted as a result. The high-resolution diurnal cycle therefore has slightly more random variability than that at SGP, even though the lengths of the time series are both several years long and offer ample sample sizes for the mean diurnal cycle (Figure

5.4). The timing of the trough and peak PBL depths during the diurnal cycle is approximately the same as at SGP: 10:00 AM and 3:00 PM local time, respectively. However, they are significantly shallower, averaging around 1 km instead of the 1.5 km average at SGP. This difference is magnified in summer. The summertime PBL diurnal cycle still has the strongest signal of CBL development, but it has the shallowest overall PBL depths. The deepest PBLs occur in winter instead, and the springtime diurnal cycle resembles the winter much more strongly than does the autumn diurnal cycle.

Meanwhile, Shouxian and Xianghe have PBL diurnal cycles that correspond to the shape and phase of the cycles at SGP and Hefei, although the shorter time series leave much more random variation in the data (Figure 5.4). Neither is long enough to make an analysis of the seasonal cycle or to determine how the diurnal cycle might change from one season to the next. However, they can be compared to the corresponding seasons at the HeRO site. The Shouxian diurnal cycle, drawn from data taken in May through December of 2008, closely resembles the summertime diurnal cycle at Hefei in phase, amplitude and mean depth. The Xianghe data comes from January through July of 2013, and may represent a more winter- and spring-like pattern for the area. Because the sites in China are subject to much higher AOD values than what is observed at SGP, these differences in the behavior of the PBL during the day point to aerosol involvement in the suppression of convection during the day, especially in summer. The fact that the wintertime PBL diurnal cycles at the HeRO and SGP sites are more similar to each other than any other season pair supports this idea; the effect of aerosol on boundary-layer stability should be weakest during the colder months, when there is little to no surface convection to suppress.

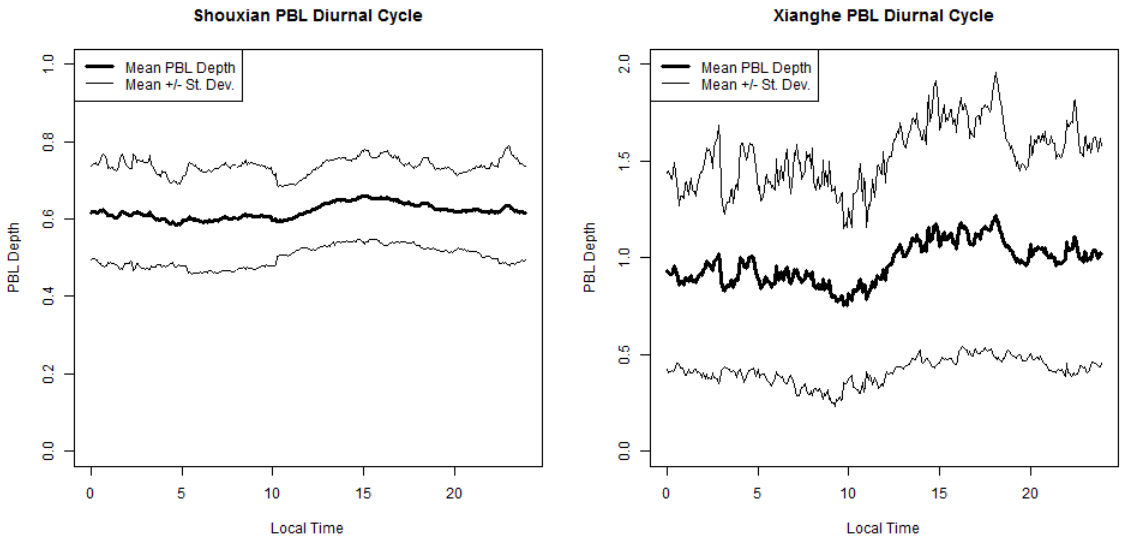

Figure 5.4. The mean diurnal cycle of PBL depths at 5-minute resolution for two shorter-term MPL deployments, Shouxian (left, 2008) and Xianghe (right, 2013). Time of day is given in hours local time (UTC+8).

The higher-than-usual random variability in the diurnal cycle at Xianghe requires some explanation. Where data are available, the PBL depth at Xianghe is analyzed at 5-minute intervals just as it is at SGP. However, many of the observation days at Xianghe leave hours-long gaps in the observation record, exacerbating the small sample size caused by the relatively short deployment; there are extended periods in which the MPL collected data for only a few hours each day, making it difficult to establish a diurnal cycle. In addition, the Xianghe MPL backscatter record shows evidence of a common problem with MPL data collection, especially in underprepared short-term deployments that have not made extensive calibration and adjustments: the temperature of the instrument was allowed to fluctuate, causing its laser signal strength to fluctuate or its optics to be distorted by the thermal expansion of the telescope. Figure 5.5 shows an

example of distorted data. The attenuation in the signal above 1 km from approximately 9:00-12:00 UTC is a natural consequence of clouds in the profile (bright white), and enhances PBL detection for boundary-layer clouds. However, the "washboard" effect of alternating lighter and darker profiles, which can be seen throughout the 24-hour observation period, is the result of a thermostat that allowed the instrument to cycle through a temperature range of several degrees Celsius, rather than any physical change in the atmospheric column. While the signal change is height-independent and has little or no effect on PBL detection, it indicates some overall unreliability in the data from the Xianghe deployment (as does the prevalence of data gaps) and may lose enough of the backscatter signal to obscure the gradient in the darkest profiles. In combination, these problems translate to noisier PBL depth retrievals over time.

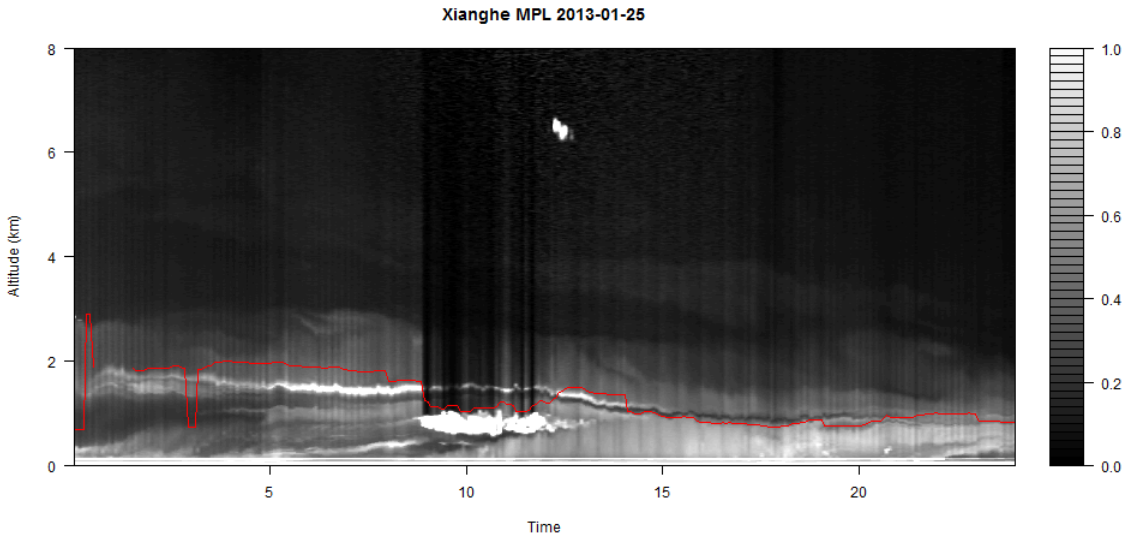

Figure 5.5. A single day of PBL depth retrievals (red) overlaid on the MPL backscatter at the Xianghe site, showing a "washboard" effect as evidence of poor telescope temperature control.

5.2 Seasonal Cycles and Interannual Variability

At the SGP site, the MPL-derived PBL depths show a strong seasonal cycle, such that the monthly median PBL depths can be fitted to a cosine curve with $R^2 = 0.90$ (Figure 4.8). This is apparent in the multiyear PBL depth record. Figure 5.6 shows the mean PBL depth overlaid on the daily range for the period 1996-2006, with a 31-day running-median filter applied to the mean, maximum, and minimum daily PBL depth. Note that the maximum and minimum daily PBL depths approximately correspond to the CBL and SBL (or RL) depths for each day, respectively. There is no linear trend on a multiyear scale and the difference between the maximum and minimum PBL depth shows no long-term change.

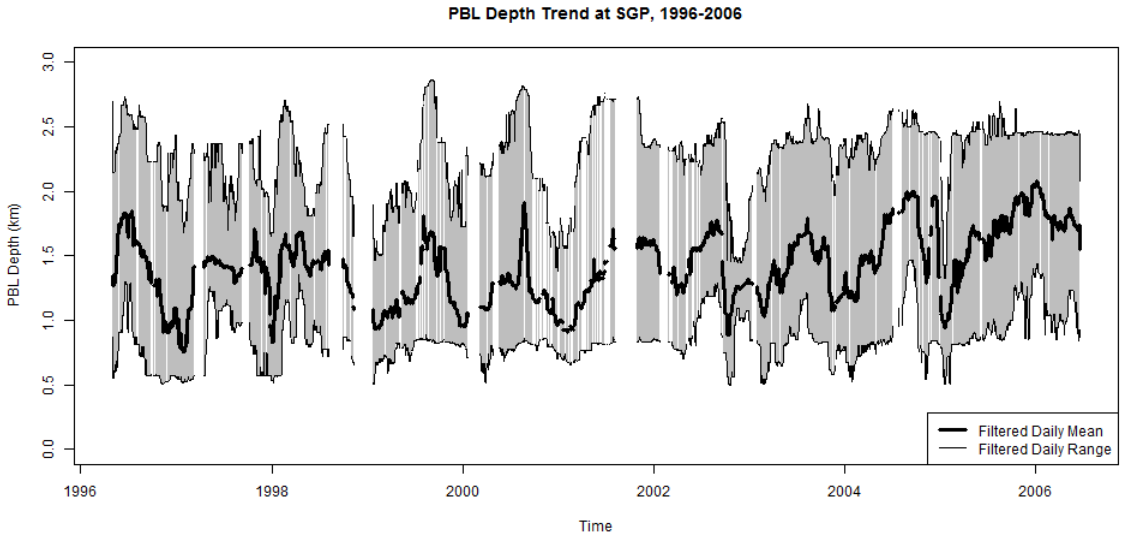

Figure 5.6. Daily mean, maximum and minimum PBL depth at SGP, with a 31-day running-median filter applied. Gaps represent periods of unreliable or nonexistent MPL data.

The daily mean AOD at the SGP site also follows a predictable seasonal cycle (Figure 5.7). Values remain below 0.1 in the winter months but become more variable in the summer, with summertime AOD values generally falling between 0.2 and 0.4. There is no long-term trend in the part of the AOD record that overlaps with the MPL observations under analysis in this project.

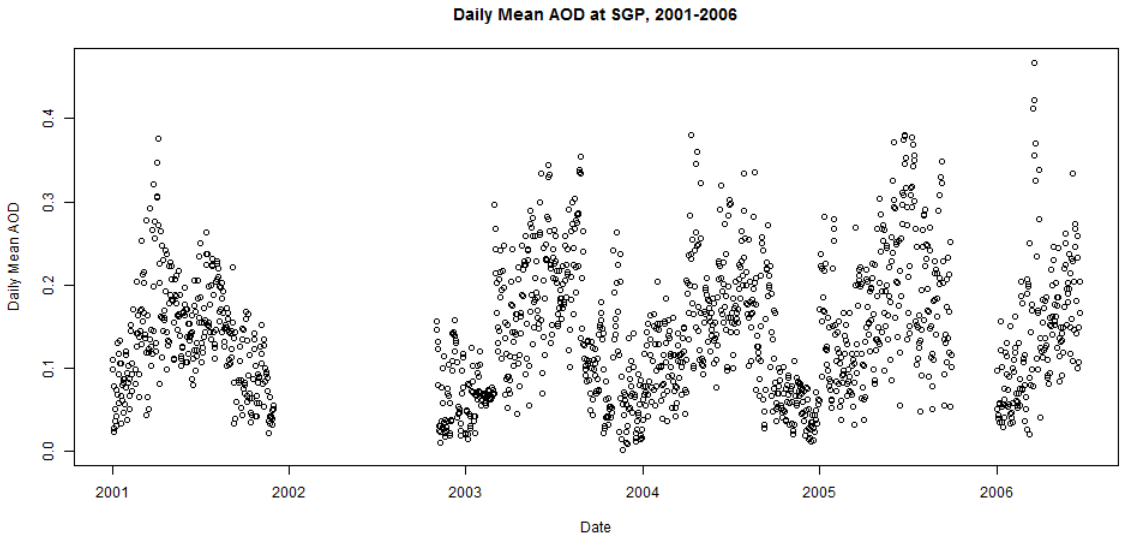

Figure 5.7. Daily mean AOD values at SGP for the period overlapping with MPL observations, 2001-2006.

While most of 2002 is missing from the data record, there is still a multiyear time series that can be compared to the MPL-derived PBL depths. The level of interannual variability is low enough that conclusions can be drawn about the seasonal cycle. However, the similarities between Figure 5.6 and Figure 5.7 also illustrate the difficulty in demonstrating that aerosol in the boundary layer suppresses convection: while there are often high springtime AOD values that correspond to seasonal peaks in aerosol long-

range transport, the peak AOD season is in summer, when surface convection is also strongest. The seasonal cycle in insolation has a far greater impact on the PBL depth than any other factor.

At the HeRO site, the monthly median MPL-derived PBL depth has a narrow peak in July corresponding to the expected summer maximum, and the shallowest median PBL depths occur in late winter or early spring. These features roughly correspond to the seasonal PBL depths at SGP, but at Hefei the seasonal cycle is much weaker and no strong periodic signal can be established (Figure 5.8).

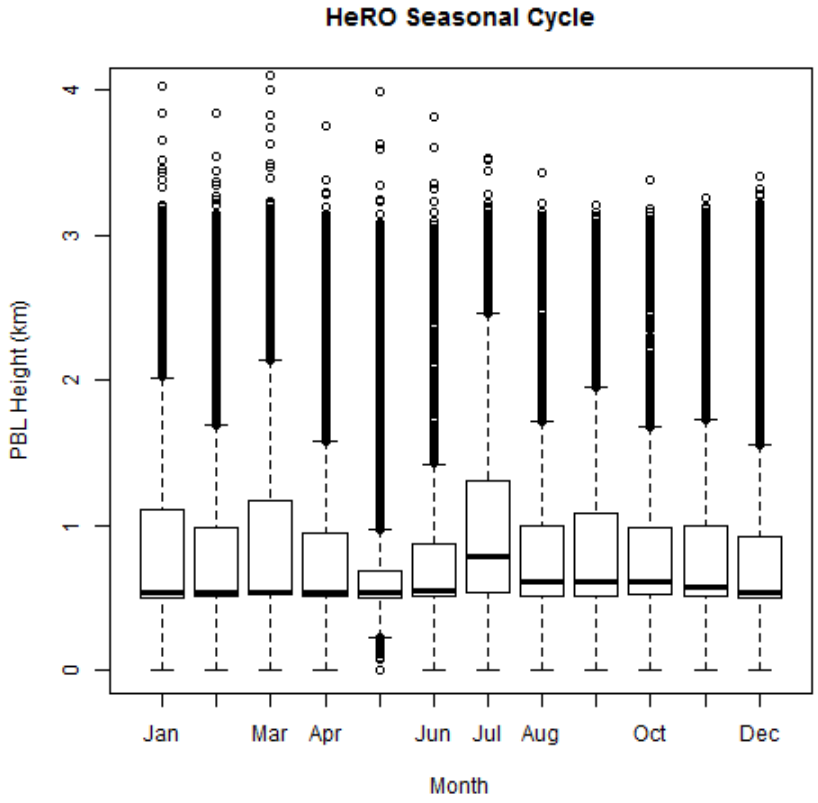

Figure 5.8. Boxplots show the distribution of MPL-derived PBL depths by month at the HeRO site, analogous to Figure 4.8.

Shallow PBL depths are common in every month except May, while PBL depths deeper than 2.5 km are mild outliers that nevertheless occur in significant numbers throughout the year. This does not necessarily mean that the PBL depth results for the HeRO site are unrealistic, but it does imply that the site experiences something other than the predictable seasonal cycle that can be seen in the multiyear record at SGP.

Instead, the multiyear record for the HeRO site shows considerable interannual variability, despite having some gaps in the record that extend for months. There is no strong seasonal cycle because differences from one year to the next, especially the peaks in the PBL depth during the spring seasons of 2005 and 2007, overwhelm any seasonal cycle that might exist (Figure 5.9). The long gap in observations in the spring of 2005 is particularly unfortunate because of the similarity before and after the gap to the behavior of the PBL in the spring of 2007. The latter peak is distinct enough from the rest of the record that a linear regression shows a significant positive trend, albeit one that certainly misrepresents the structure of the PBL depth; it is unlikely that this peak represents a long-term change in the behavior of the PBL at Hefei.

Considering the maximum CBL depth alone, as the most reliable PBL depth in a typical diurnal cycle, the same contrast between SGP and HeRO appears. At SGP (Figure 5.6) there is little interannual variability and no apparent long-term trend in the maximum CBL depth, though the seasonal cycle is less apparent than in the daily mean PBL. At the HeRO site (Figure 5.9) the deepest CBLs occur mainly in the period 2005-2007, with periods of much shallower CBLs that do not fit a predictable seasonal cycle. While there is no defined linear trend, realistic or otherwise, there is a much wider range in CBL depths that could be considered typical of a given season at Hefei.

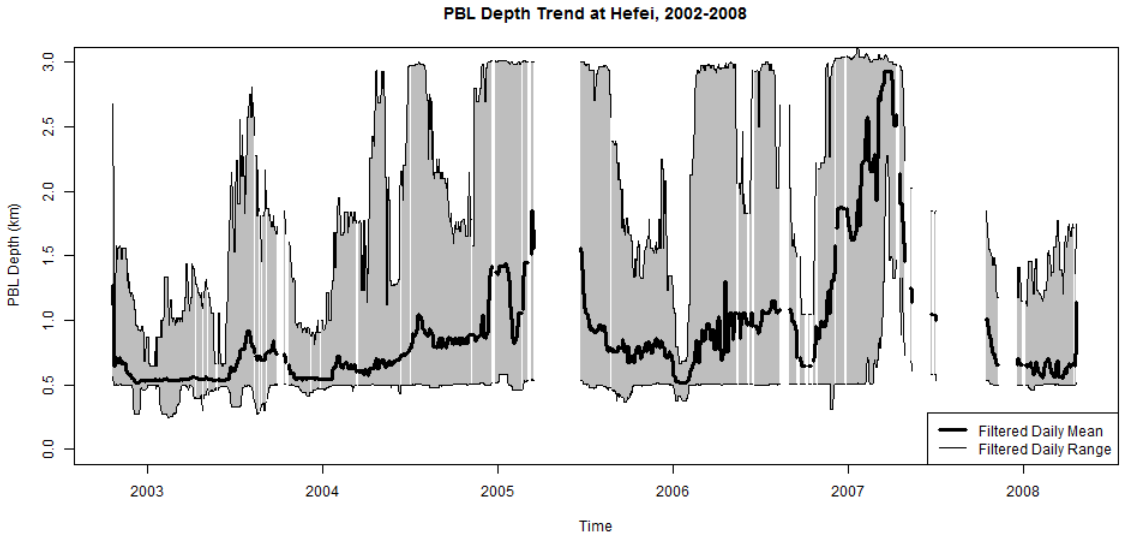

Figure 5.9. The same as Figure 5.4 but at Hefei.

The causes for this interannual variability cannot be determined from the CBL depth, or the underlying MPL data, alone. Because the available AOD data only begins in 2007, it is not even possible to determine whether changes in aerosol loading correspond to the seasonal cycle or to features found in the MPL data from the site. Hefei is subject to a monsoon pattern that produces extended periods of precipitation in early summer; this is one of many processes that may make the synoptic conditions less consistent from year to year. Nevertheless *Wang et al.* [2014], a later study at the same site, was able to establish a rough seasonal cycle for AOD for the period 2007-2013 (Figure 5.10). It's equally possible that the PBL peaks in 2005 and 2007 correspond to aerosol rainout, or to synoptically driven differences in the cloud base height.

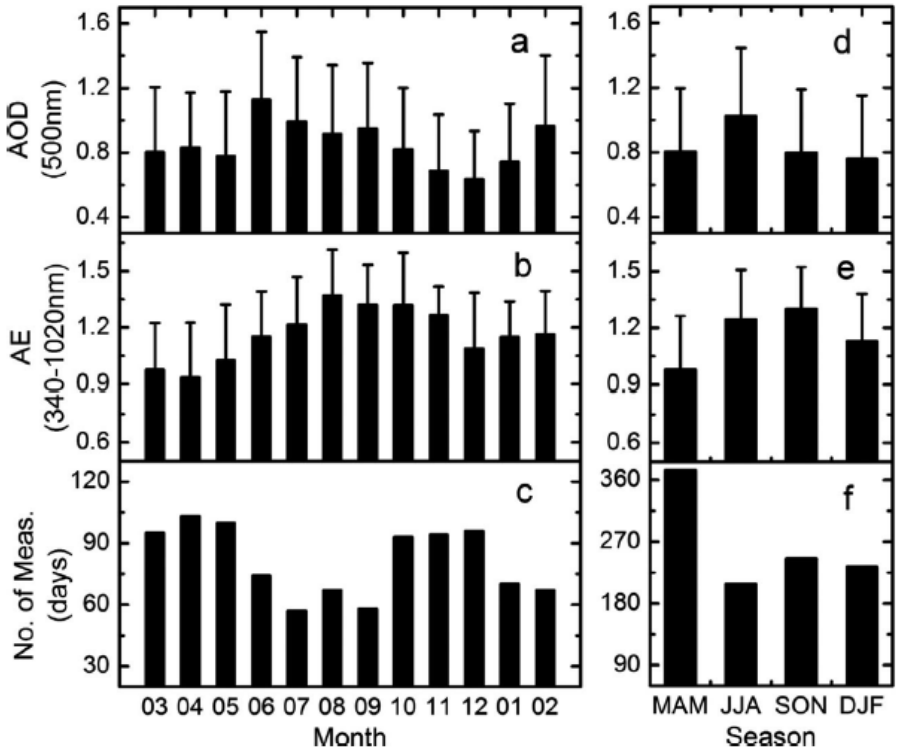

Figure 5.10. From *Wang et al.* [2014], monthly and seasonal mean 500-nm AOD (a,d), mean Angstrom exponent (b, e), and number of measurements (c, f), at Hefei, 2007-2013.

Summer at Hefei is characterized by the highest AOD values of the year (and fewest available measurements). The seasonal diurnal cycle in Figure 5.3 suggests that summer is also characterized by the shallowest PBL depths despite the presence of surface convection, but the monsoon cycle and the high interannual variability at the site cast doubt on the effectiveness of dividing the data into four seasons for analysis. The behavior of the AOD and PBL depth in early summer is very different from their behavior in late summer, and the early summer especially shows signs that it depends on other factors for that particular year. However, there is circumstantial evidence in these results, and especially when compared to the generally deeper and more predictable PBLs

at SGP, that aerosol loading affects the PBL depth and may suppress convection at Hefei when AOD values are high.

Chapter 6. PBL Depth and AOD

6.1 WRF-Chem Results for April 2004 at SGP

The diurnal cycle of the PBL depth is an important consideration when comparing PBL depth to AOD. The aerosol loading of the mixed layer tends to change on slower time scales than the PBL depth, and a direct comparison without regard for the time of day the observations were taken risks conflating the surface convection-based PBL development with the factors that are under evaluation for their effect on it. For this reason, the AOD measurements in this chapter from SGP and Hefei are always the daily mean values, while the PBL depths are separated by the time of day they were taken. For the part of this study dealing with the WRF-Chem model run described in Chapter 2, the daily mean AOD values are compared to PBL depths from various sources at standard radiosonde launch times: 00:00 UTC, 06:00 UTC, 12:00 UTC and 18:00 UTC. At SGP, the 00:00 UTC launch corresponds to a local time of 6:00 or 7:00 PM and can be interpreted as the peak CBL depth; 12:00 UTC corresponds to early morning and is close to the expected time of the shallowest SBL depth. 06:00 UTC and 18:00 UTC are transitional times corresponding to overnight and midday PBLs, respectively.

The chosen PBL intervals allow output from the WRF-Chem run to be used alongside radiosonde data from the site, which is important because two forms of output were considered: the YSU scheme PBL depths, and the modeled θ_v profile for the SGP site (the center of the model domain). In effect, the latter output is a simulated instrument: the same information that a radiosonde would measure in the real world, and in the case of the SGP site, corresponding to actual radiosonde measurements made during April 2004. Accordingly, this output can be used with the combined algorithm

from Chapter 3 to produce PBL depths based on the thermodynamic definition of the PBL, in contrast to the Richardson number method-based derivation of the YSU scheme PBLs. Figure 6.1 shows the resulting comparisons between model-output PBL depths and the observed daily mean AOD side by side.

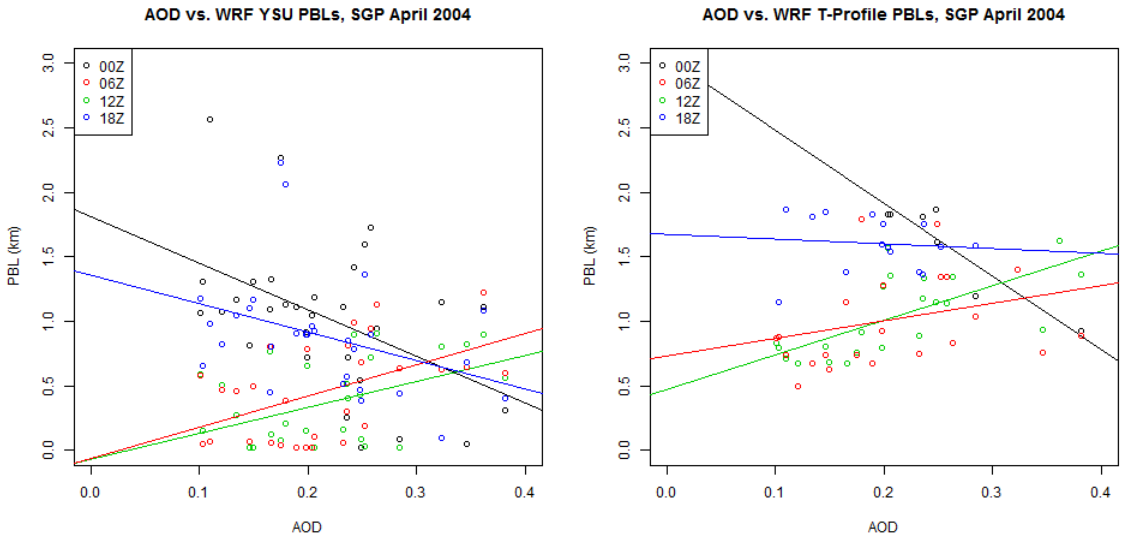

Figure 6.1. AOD vs. PBL depth for model-derived PBL depths at the radiosonde launch interval. Left, YSU scheme; right, simulated radiosonde.

While the linear correlation between PBL depth and AOD is weak for any given time of day—the highest R^2 values found by linear regression were borderline significant at approximately 0.3—the 00:00 UTC PBL depths show a consistent decline with higher values of AOD, while the 12:00 UTC PBL depths show a weaker positive correlation. No correlation between PBL depth and AOD should be expected overnight, when there is no insolation to be affected by the radiative forcing of aerosols.

The observations for April 2004 at SGP include PBL depths detected by two methods, first the method from *Liu and Liang* [2010] and then the method described in

Chapter 3, which is also published in *Sawyer and Li* [2013] and is referred to that way to distinguish the two sets of PBL results. The two methods return results that are approximately as similar to one another as the instrument comparisons from Chapter 4. This can be seen in Figure 6.2, which compares the two methods for the radiosonde launches corresponding to the time of the WRF-Chem run; it is representative of the comparison of the full set of results. The *Sawyer and Li* [2013] algorithm does not distinguish between PBL regime types and tends to detect deeper SBLs than the *Liu and Liang* [2010] algorithm, but they are both effective methods for PBL depth detection.

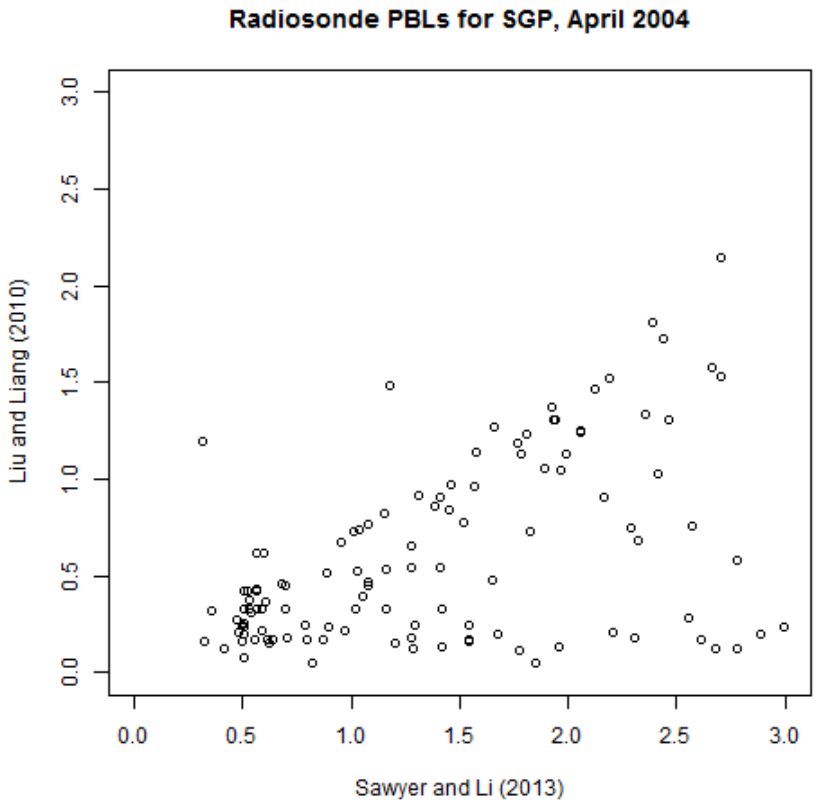

Figure 6.2. Radiosonde-derived PBL depths from two different algorithms, using observations taken from the simulated period at SGP.

Figure 6.3 shows the comparison between the daily mean AOD at the SGP site for April 2004 and the two sets of radiosonde-derived PBL depths. As in Figure 6.1, the 00:00 UTC launch time is associated with PBL depths that get shallower as AOD increases, while there are weaker positive correlations between AOD and PBL depth for the overnight and early-morning launch times. The similarity in the findings among all four comparisons shows that the PBL depths are valid and that the relationship between daytime CBLs and the AOD is probably different from the relationship between overnight SBLs and the AOD. However, the radiative effect is weak compared to other variations in PBL depth, and a data set covering much more than the 30 days of the WRF-Chem run would be needed to fully quantify the relationship.

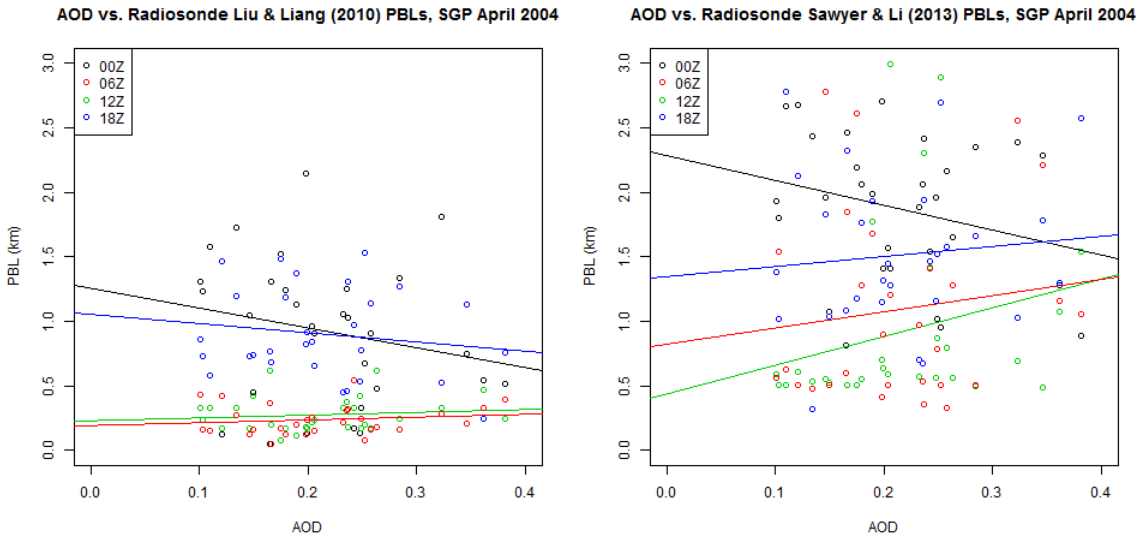

Figure 6.3. AOD vs. PBL depth for radiosonde-derived PBL depths from *Liu and Liang* [2010] (left) and *Sawyer and Li* [2013] (right).

6.2 PBL Depth vs. AOD at SGP and HeRO

In data sets much larger than the 30-day WRF-Chem run, scatterplots obscure the relative frequency of different values. One solution to this problem was to examine the distribution of PBL depths for different daily mean values of AOD, as shown in Figure 6.4: each boxplot shows the PBL depths for a limited range of AOD values. Both sites show at least a slight decrease in PBL depth with AOD, especially in a loss of deep PBLs while the very shallow PBL depths remain unaffected. At the HeRO site, the effect is much more dramatic than it is at SGP; the range of AOD values is more than four times the range at SGP, and there is a wider sampling of polluted conditions. In fact the HeRO time series contains only one day with a mean AOD value less than 0.25, while AOD values above 0.25 are somewhat rare at SGP.

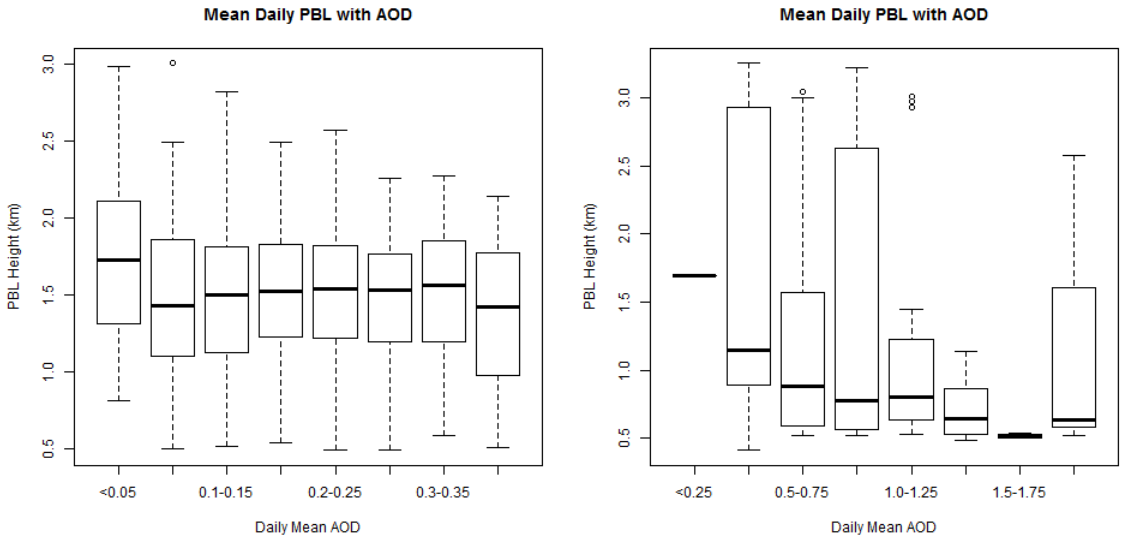

Figure 6.4. Boxplots showing the distribution of PBL depths with increasing AOD, at SGP (left) and Hefei (right).

Furthermore, at the HeRO site the relationship between PBL depth and AOD is limited to CBLs, while SBLs show no pattern with changing AOD. Figure 6.5 constructs similar boxplot series for the daily maximum and daily minimum PBL depths at Hefei, corresponding respectively to the mature daytime CBL and nocturnal SBL depths for each day with AOD data. The AOD values are again the daily mean, not necessarily the value at the time of day corresponding to the maximum or minimum PBL depth. While the median CBL depth decreases from 3 km on the cleanest day to less than 1.5 km on days with AOD above 1.75, the median SBL depth remains close to 500 m regardless of the aerosol conditions. This indicates that higher AOD values are associated with suppressed convection and shallower CBLs, but it serves as exploratory statistics rather than a method for quantifying the relationship between AOD and PBL depth. A different statistical method is needed to compare the strength of the observed relationship to the model results discussed in section 1.3.

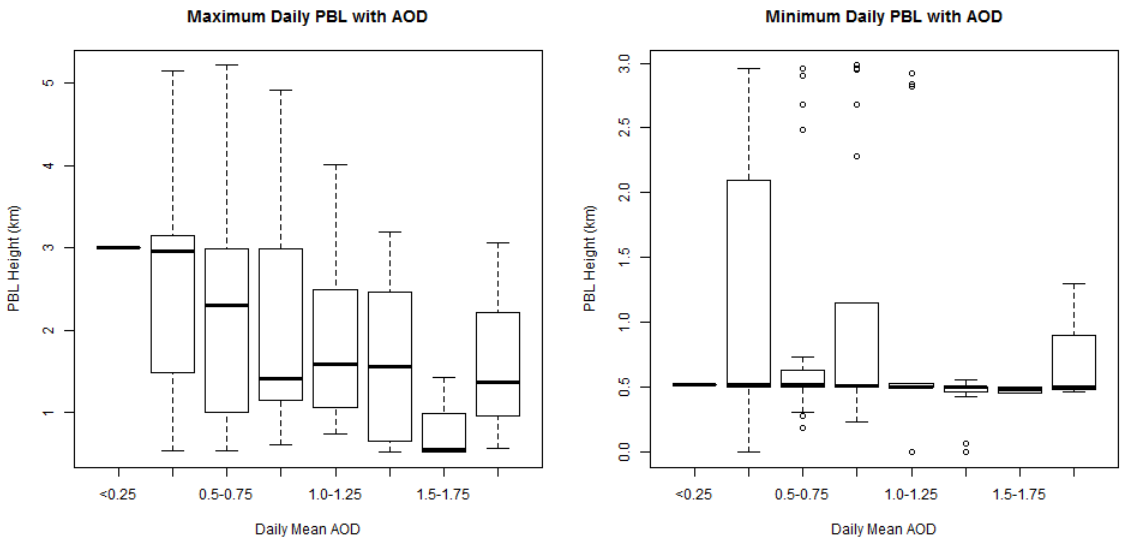

Figure 6.5. Boxplots showing the distribution of maximum daily CBL depth (left) and minimum daily SBL depth (right) at the HeRO site.

Since a scatterplot obscures features of the data and exploratory methods lack quantitative rigor, it is helpful to use probability density functions instead. All probability density function methods find a continuous curve to represent the distribution of data, whether by assessing the fit of a prescribed curve or by estimating one directly from the data. As a form of the latter method, a kernel density estimate allows the fewest possible prior assumptions about the structure of the probability density. For two variables, this takes the form

$$\hat{f}(\boldsymbol{x_0}) = \frac{1}{nh_1h_2}\sum_{i=1}^{n} K\left(\frac{x_0 - x_i}{h_1}\right) K\left(\frac{y_0 - y_i}{h_2}\right) \quad , \qquad (6.1)$$

where *h* is a smoothing parameter for each variable and *K* is the kernel function [*Wilks*, 2006], in this case the Gaussian function shown below:

$$(2\pi)^{-\frac{1}{2}} \exp\left[-\frac{t^2}{2}\right] \quad . \qquad (6.2)$$

The result is analogous to a two-dimensional probability histogram except that it is continuous, not subject to arbitrary binning decisions, and more readily represented as a contour plot. The volume under the surface is an estimate of the probability of the two variables falling within a given range, with the total volume equal to one.

Figure 6.6 shows the resulting distributions for daily mean AOD and daily maximum PBL depth (representing the peak of the CBL) at SGP and the HeRO site. One immediate advantage over the boxplots in Figure 6.4 is that the kernel density estimate

reveals bimodal and clustered behavior that was not visible in the exploratory plots. Namely, for the HeRO site there seems to be a cluster of clean, deep PBLs in the upper left of the plot that is distinct from the rest of the data. This is not due to clouds in the MPL profile, but appears to occur under clear skies in winter and spring. It may be possible that despite efforts to eliminate blank and low-signal profiles from PBL detection, there are very clean days in the record for which the algorithm has insufficient backscatter data to correctly identify the PBL depth, and returns values near the top of its analysis range instead. However, none of the PBL depths included in this analysis showed the clustering around the highest possible wavelet covariance-derived first guess that earlier versions of the algorithm produced under such circumstances. It is more likely that the backscatter feature being marked as the PBL is real, especially since using the daily maximum tends to exclude overnight residual layers and capping inversions that may be detected by mistake.

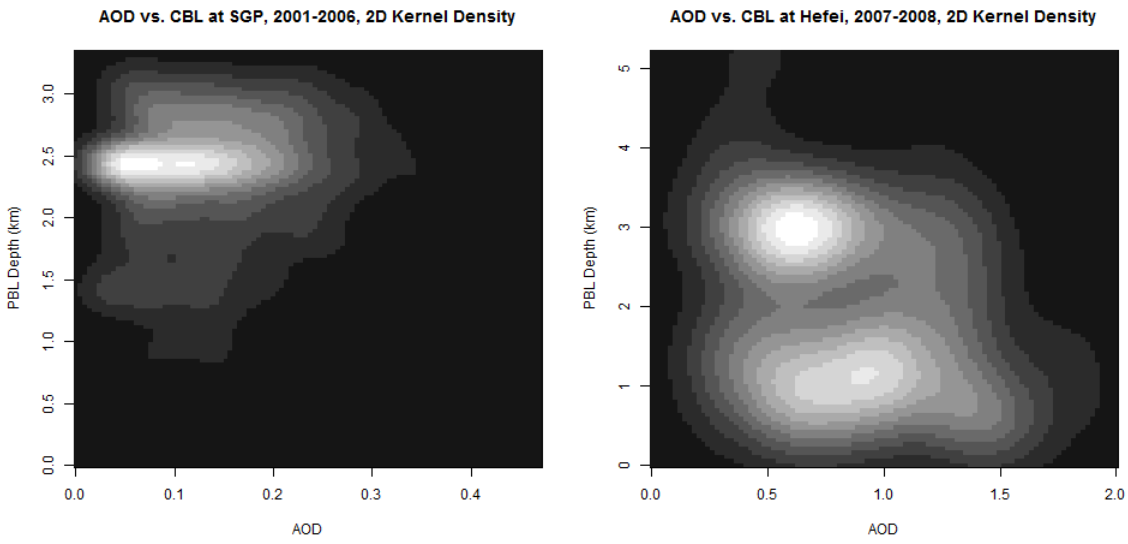

Figure 6.6. Kernel density estimates of daily mean AOD vs. daily maximum PBL depth at SGP (left) and Hefei (right).

Figure 6.7 shows the same kernel density estimates for AODs and CBL depths measured in December, January and February only. The cluster of clean, deep CBLs is now more clearly visible at SGP than at HeRO, while the results at the HeRO site confirm expectations about shallow, unchanging wintertime PBL depths (possibly exaggerated by the overlap limit of the lidar in the case of the shallowest CBL values). At SGP, AOD values tend to be lower during the winter months than at other times of year; at Hefei, the AOD values occur throughout the full observed range.

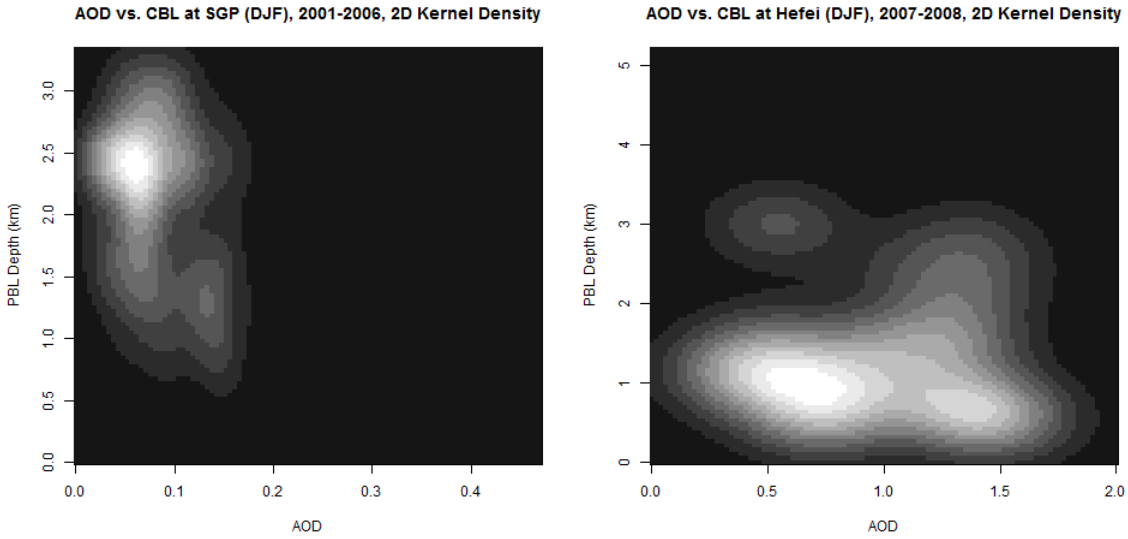

Figure 6.7. Kernel density estimates of daily mean AOD vs. daily maximum PBL depth at SGP (left) and Hefei (right), for the winter months only.

More polluted days occur at SGP in June, July and August; at the HeRO site, summertime tends to have much lower AOD values than the winter months (Figure 6.8). At both sites, any relationship between AOD and CBL depth seems slight, whether because the CBL depth varies less than in other seasons (at SGP) or because the AOD

value barely changes (at Hefei). At the HeRO site, the PBL depths again form clusters that may indicate another factor affecting both PBL depth and AOD. The season-dependent distributions of CBL depth and AOD make the comparison between the two variables difficult on a season-by-season basis.

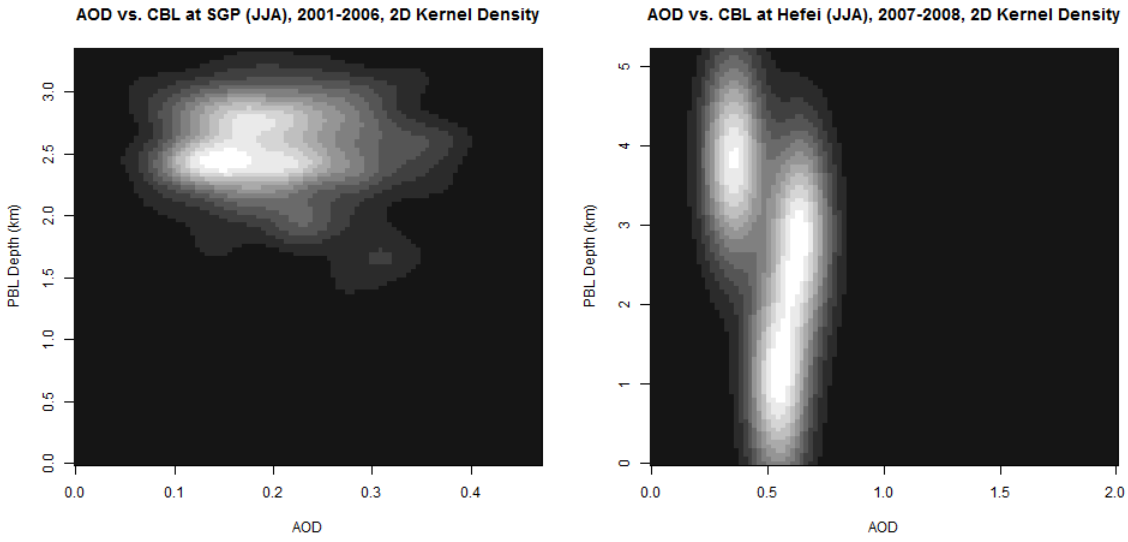

Figure 6.8. Kernel density estimates of daily mean AOD vs. daily maximum PBL depth at SGP (left) and Hefei (right), for the summer months only.

Because the two-variable kernel density estimate considers the frequencies of PBL depth and AOD equally, it is especially difficult to determine the distribution of PBL depths for rare values of AOD in any given subset of the observation record. Since this study is interested in how the PBL depth changes with AOD, including the possibility of future AOD values that may be unusual in the current data record, the existing AOD distribution is less helpful than how it relates to the PBL depth distribution. It would be better to assess the PBL depth given a particular value of AOD, and to use

conditional probability instead of treating both variables equally in the kernel density estimate.

In the most general possible terms the conditional probability is given by the equation

$$Pr\{E_1|E_2\} = \frac{Pr\{E_1 \cap E_2\}}{Pr\{E_2\}}, \tag{6.3}$$

where E_1 and E_2 are the two variables under consideration. It follows that the conditional probability of PBL depth given AOD can be determined by dividing the two-dimensional kernel density estimate by the one-dimensional estimate for AOD.

The Nadaraya-Watson Estimator, first described by *Nadaraya* [1963] and *Watson* [1964], adapts the principles of conditional probability to kernel density estimates. It is given by the equation

$$\hat{f}(y|x) = \frac{\sum_{i=1}^{n} K_{h_1}(y-y_i)K_{h_2}(x-x_i)}{\sum_{i=1}^{n} K_{h_2}(x-x_i)}, \tag{6.4}$$

where *h* and *K* are again the smoothing parameter for each variable and kernel function, respectively, as in equation 6.1. For the version of the Nadaraya-Watson estimator that is available through the *ksmooth* function in R, h_1 is set equal to h_2 to form a single bandwidth *h* that can be set by the user. The smaller the bandwidth, the more complex the shape of the ensuing estimate and the more responsive to small-scale changes; the optimal bandwidth value minimizes the average error of the estimate.

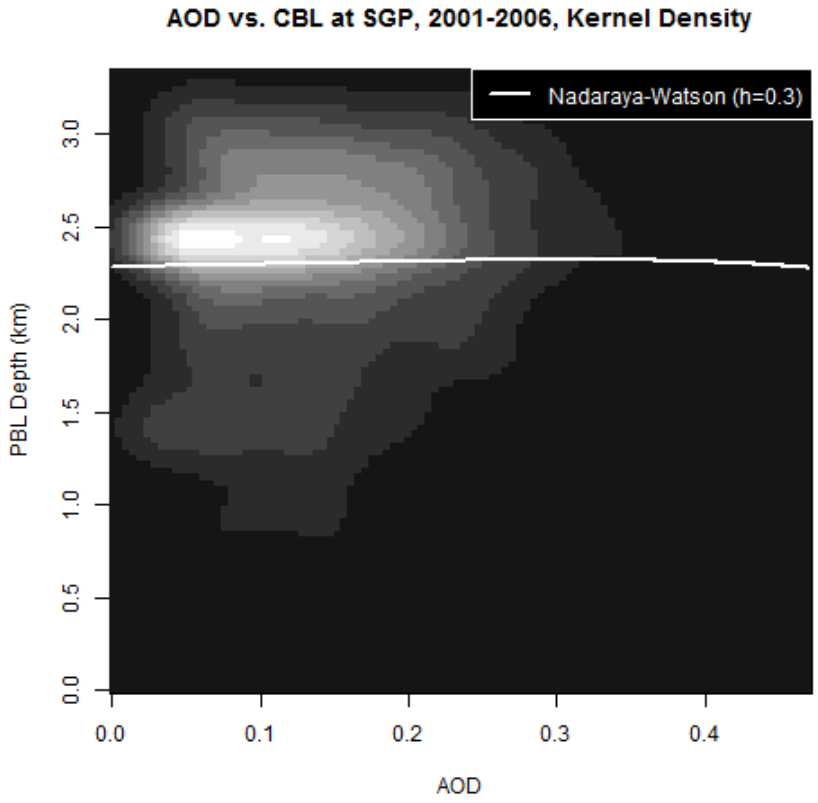

Figure 6.9. Mean daily AOD vs. maximum daily PBL depth at SGP. The Nadaraya-Watson estimator is overlaid on the kernel density estimate.

The Nadaraya-Watson estimator at the optimum bandwidth has been overlaid on the two-dimensional kernel density estimates for Figures 6.9 through 6.12. At the SGP site, the optimal bandwidth results in a shallow curving fit with a slightly increasing trend, equivalent to less than 40 m per unit AOD (Figure 6.9). When the same analysis is divided into seasons, however, a positive trend appears only in autumn; for the summer months the trend shows a 180 m decrease in CBL depth for each unit increased AOD (Figure 6.10). While this is a small trend compared to the average PBL depth, it roughly agrees with the findings of the *Xing et al.* [2015] AMS talk: each unit of increased AOD was found to cause daily mean PBLs that were shallower by 69 to 79 m. With a range of

0.4 in AOD values, this predicts that the lowest-AOD days should have PBL depths approximately 30 m deeper than those of the days with the highest AOD values: a small difference that is difficult to confirm through observation. When using the daily mean PBL as *Xing et al.* [2015] did rather than the maximum, the Nadaraya-Watson estimator found that the PBL depths at SGP changed by approximately 50 m instead, a slightly stronger relationship than the model predicted.

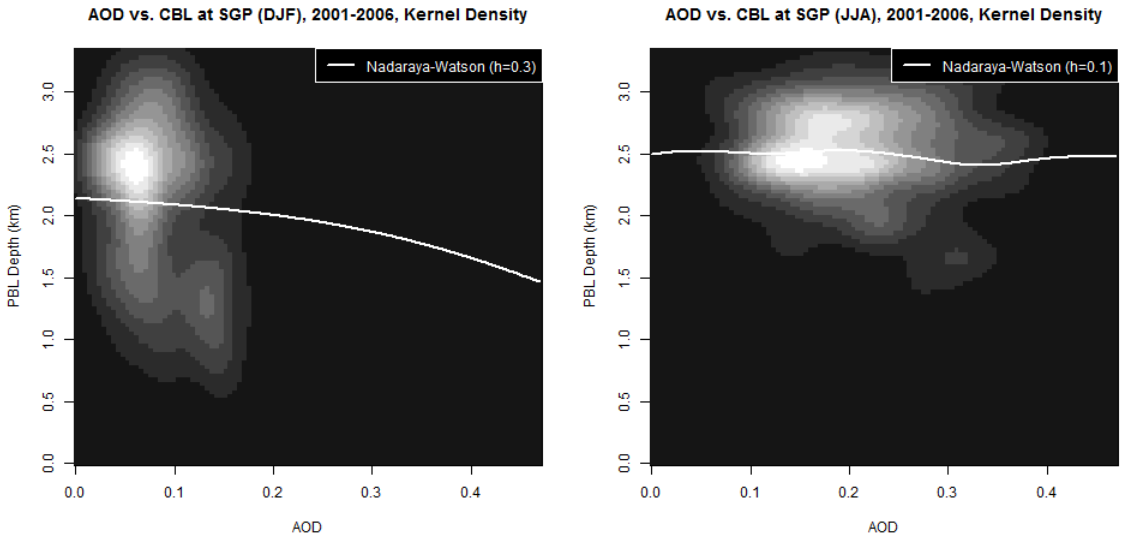

Figure 6.10. The Nadaraya-Watson estimator overlaid on the daily mean AOD vs. the daily maximum PBL at SGP, during winter (left) and summer (right).

In the same way, the *Xing et al.* [2015] linear relationship between AOD and PBL depth predicts a difference between the aerosol-free and most polluted days at the HeRO site of almost 150 m. The Nadaraya-Watson estimator finds a difference of closer to 880 m, or approximately 440 m per unit AOD. When the same relationship is found for AOD vs. the daily maximum PBL (Figure 6.11) the rate is 580 m per unit AOD.

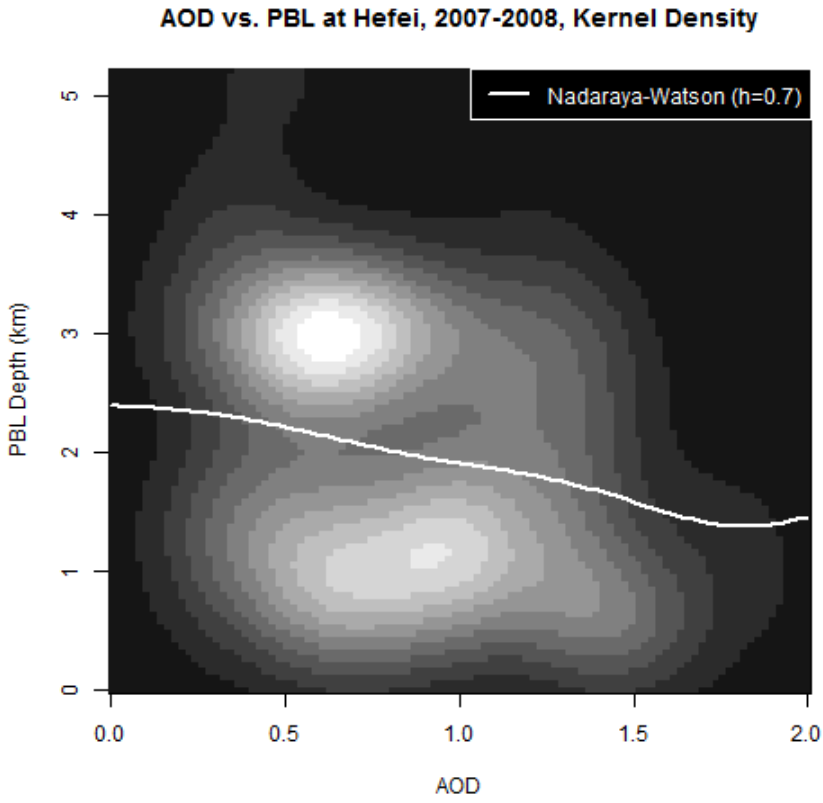

Figure 6.11. Mean daily AOD vs. maximum daily PBL depth at Hefei. The Nadaraya-Watson estimator is overlaid on the kernel density estimate.

The steepness of this slope is certainly due to the bimodal behavior of the PBL depths at Hefei. However, the negative trend remains even if the entire upper-left cluster of PBL depths is considered unreliable and removed from the analysis. As seen in Figure 6.12, the Nadaraya-Watson estimator cutting through the center of the lower cluster retains a negative slope of about 160 m per unit AOD. The cleanest days are estimated to have a peak CBL depth of about 1.2 km, while the most polluted days have peak CBLs shallower than 900 m.

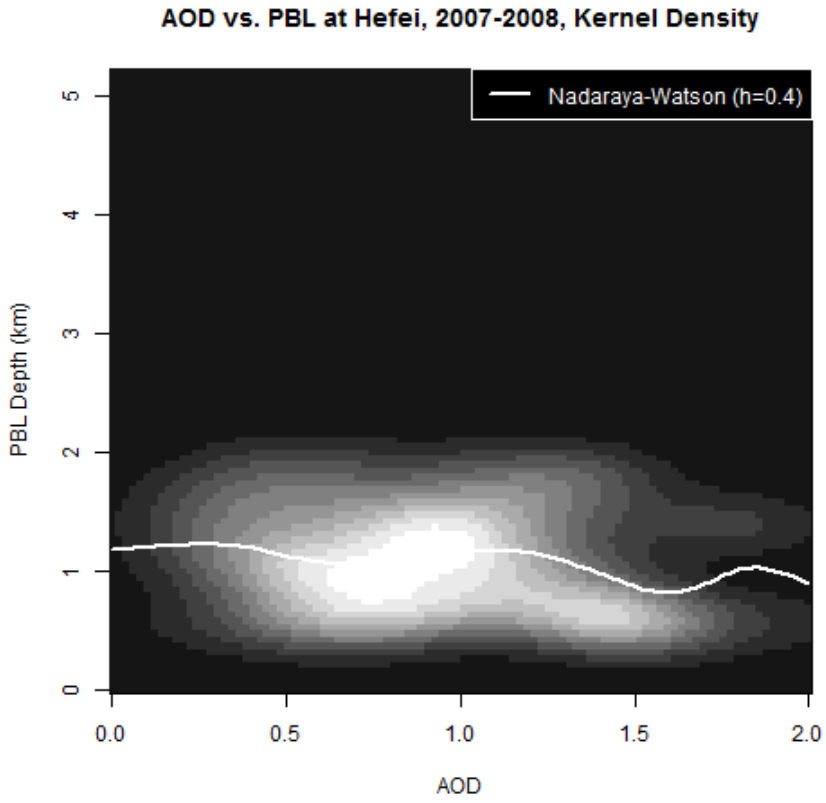

Figure 6.12. As in Figure 6.10, but with all PBL depths above 2.0 km removed.

While a greater decrease in PBL depth was expected at Hefei than at SGP in absolute terms, it is not clear why the rate of decrease per unit AOD at Hefei is more than twice the rate at SGP. The sensitivity of PBL depth to AOD undoubtedly varies with a number of other factors. One of these is SSA, but the low AOD values at SGP make it uncertain whether there is enough contrast between SGP and HeRO to analyze; these sites do not provide a good test of the effect found in *Yu et al.* [2002]. However, that study and others have emphasized the importance of moisture content and the distribution of aerosol through the column, where some of the radiative effect may be occurring in the

free troposphere instead of within the PBL. These factors are discussed in Chapter 7 as directions for future work.

6.3 Operational Radiosonde and Satellite-Based AOD

While the shortcomings of operational radiosonde for PBL detection are discussed in Chapter 5, the network has denser spatial coverage in China than any other ground-based measurement network of atmospheric profiles. This feature becomes crucial when working with satellite data, such as AOD measurements taken from the Moderate Resolution Imaging Spectroradiometer (MODIS) instrument aboard the NASA Aqua satellite. Figure 6.12, created by Jianping Guo, demonstrates the geographic coverage of satellite-based AOD measurements over China and identifies four typical pollution "hot spots" for further study. These are the North China Plain (NCP), the Yangtze River Delta (YRD), the Sichuan Basin (SCB) and the Pearl River Delta (PRD). Three radiosonde sites from each region provide a comprehensive perspective of each "hot spot."

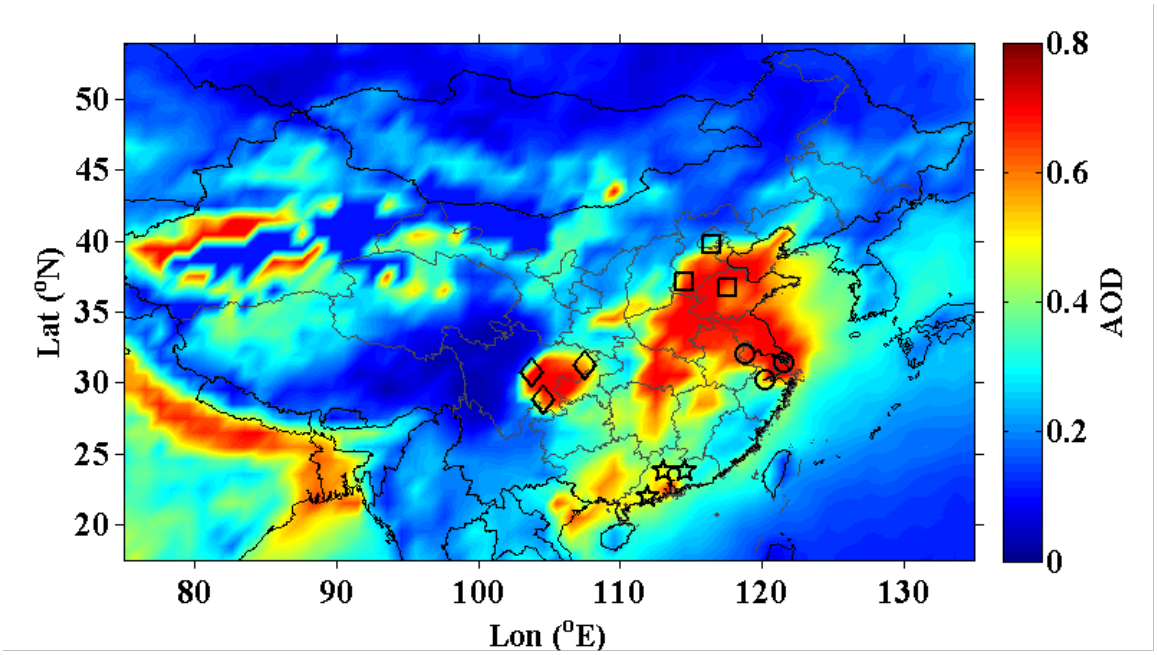

Figure 6.13. AOD measurements from MODIS/Aqua for the geographic area coinciding with the operational radiosonde network in China. Radiosonde sites within four pollution "hot spots" are shown: squares "□" for NCP, circles "○" for YRD, diamonds "◇" for SCB, and five-pointed stars "☆" for PRD.

Over the period 2011-2013, each radiosonde site conducted over 2,000 launches, mostly at 00:00 and 12:00 UTC (8:00 AM and 8:00 PM local) but with a few launches at 06:00 and 18:00 UTC (2:00 PM and 2:00 AM local). Guo used the PBL detection code from this study to analyze the radiosonde profiles for PBL depth. Operational observations of visibility are used to divide the profiles into thirds, with the highest third (visibilities above 15 km at YRD, NCP and SCB or 18 km at PRD) considered "clean" atmospheric conditions and the lowest third (visibilities below 7 km at YRD, 10 km at NCP and SCB and 12 km at PRD) considered "polluted." While this binary comparison cannot reveal a linear relationship between PBL depth and AOD, the contrast in the distribution of PBL depths is more clearly visible. Figure 6.13 shows the difference in the likelihood of a range of PBL depths under clean and polluted conditions. The strength of

the apparent effect varies from one region to the next, but all four regions show an increased probability of shallow PBL depths and a decreased probability of deep PBL depths under polluted conditions as compared to clean conditions. This is consistent with expectations that higher AOD values cause suppressed surface convection and shallower overall PBL depths.

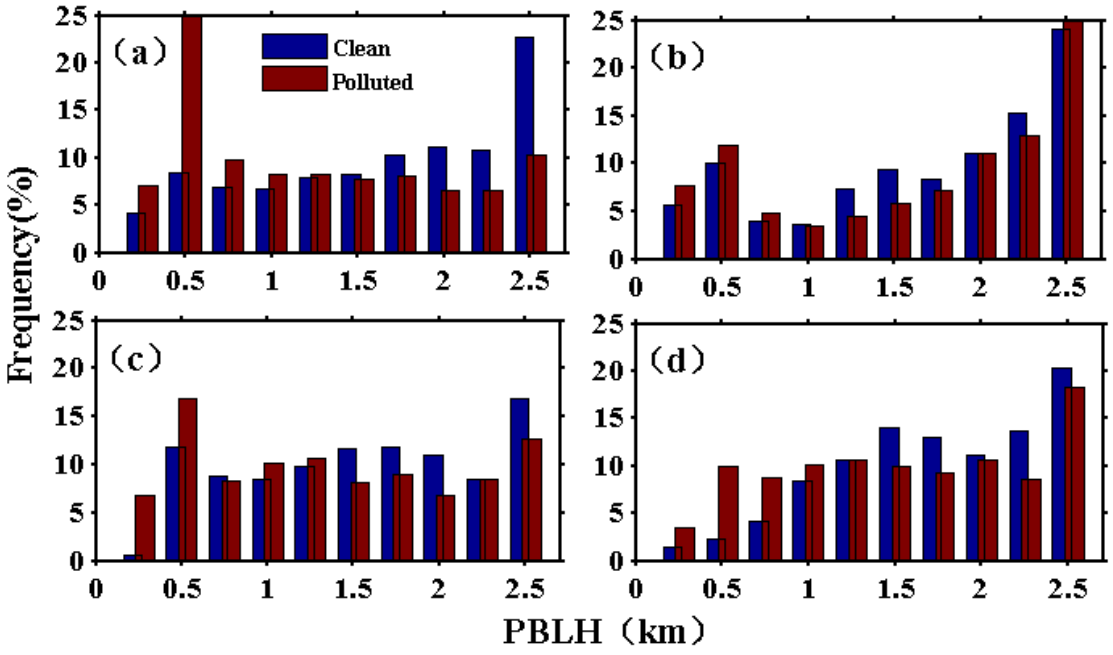

Figure 6.14. Probability distribution function of PBL depth under clean (blue) and polluted (red) conditions, for the regions a) NCP, b) SCB, c) YRD and d) PRD.

The extent of the difference in PBL depth between clean and polluted conditions varies spatially; the smallest difference is observed at PRD, where it should be noted that the threshold for polluted cases was significantly higher than for the other three regions. Because the determination of "clean" and "polluted" days in Figure 6.13 is relative to each site, regional differences in the absolute pollution levels during clean and polluted

cases are undoubtedly a factor. However, these results qualitatively confirm the findings at the MPL sites for a wider variety of locations, showing that the relationship between PBL depth and AOD is not an artifact due to limited observations.

Chapter 7. Future Work

7.1 Varying SSA, Humidity and Clouds

While the SGP and HeRO sites used in this study were necessary because of their long MPL instrument records and contrasting AOD, neither site shows much internal variation or contrast from one another in SSA that can be demonstrated conclusively. Since the reflectivity and absorptivity of aerosols are at least as important as AOD to the radiative impact and the resulting behavior of the PBL, this rather unrepresentative view of aerosols is problematic. High SSA values are also often linked to moisture content, and boundary-layer moisture has its own impact on PBL development [*Garratt et al.*, 1990; *Yu et al.*, 2002]. *Garratt et al.* [1990] mentioned that the formation of fog can alter the stability of the PBL. Humidity soundings are available at the SGP site from radiosonde and AERI, but not at the other MPL deployments, and it is by no means certain that this data would be available from a site that experienced high contrast in SSA values or simply more absorbing aerosols. Raman lidar, which is capable of measuring both aerosol backscatter and vertical moisture profiles, may offer the best of both worlds, but there are few long-term deployments of this instrument in the US and China.

As the mention of fog makes clear, there is considerable overlap in the radiative effects of aerosol, moisture, and clouds. The aerosol direct effect is not the only process affecting the behavior of the PBL, and changes in the PBL depth will also change boundary-layer clouds. Cloud bases are easily detected by MPL (and already included in this project); at the SGP site, aerosol loading has been shown to affect cloud development in a previous study by *Li et al.* [2011]. For convective clouds, the PBL top and the lifting condensation level are linked, and aerosol affects them together. For stratocumulus

clouds, the possibility of decoupling is a further complication that cannot be addressed by MPL—and has an ambiguous place in the thermodynamic definition of the PBL. Future work must find a way to reconcile the effects of aerosol on boundary-layer clouds with competing PBL definitions and the limitations of different measurement types.

7.2 An Alternative Modeling Approach

Previous modeling studies have simulated the PBL depth using the turbulent definition, parameterizing the PBL depth in a way that does not explicitly simulate the convective processes that are affected by aerosol radiative effects within the PBL. As computational resources become available, there have been efforts to model convective plumes and associated processes more directly. Some of this effort is directed at improving the simulation of convective cloud development and precipitation [*Rio et al.*, 2013], but because boundary-layer cloud processes are intimately linked to the behavior of the PBL, an advance to one process will also improve the other as long as the model aims for greater overall realism. *Rio et al.* [2013] suggests basing boundary-layer cloud schemes upon the available lifting power from the surface, rather than convective available potential energy; this requires a more direct approach to convective thermals. *Gentine et al.* [2013] uses probabilistic bulk convection to parameterize surface convection, resulting in a more flexible simulation of the entrainment at the boundary layer top and a unified approach to clear-sky and cloud-topped PBLs. Both these studies evaluate their PBL results by comparing precipitation rates to observations; were direct

observations of the PBL depth more widely available, they might be able to make better assessments.

The close connection between the behavior of the PBL and surface convection has led to modeling approaches that treat them as a single system. *Cheinet* [2003] introduced a one-dimensional model framework for clear-sky surface convection, which is continued for cloudy cases in *Cheinet* [2004]. While single-column models have been used to study chemical transport and the PBL depth before now [*Park et al.*, 2001], Cheinet's approach is different in that it allows convective plumes to be modeled explicitly, which has been done extensively to study cloud development but never for the purposes of PBL studies. This is in contrast to the turbulence scheme used to parameterize boundary-layer processes in weather and climate prediction models including WRF-Chem: not only is it able to simulate PBL development in greater detail, but in its recognition of buoyancy as the most important factor in vertical mixing, it makes use of the thermodynamic definition rather than the turbulent definition of the PBL. In many ways, this modeling approach is better suited to the evaluation of PBL depths from a single site's worth of ground-based observations than previous attempts to fit a regional climate model to the observations. Figure 7.1 illustrates the model processes from *Cheinet* [2003] for dry (unsaturated) convective plumes.

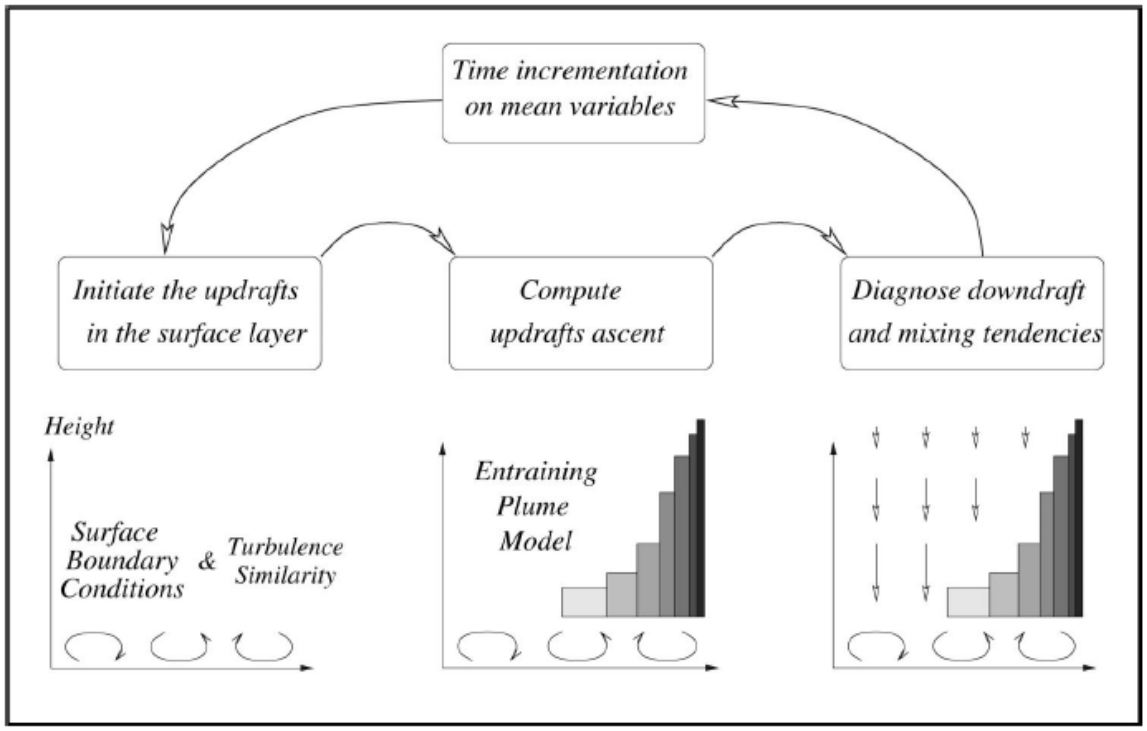

Figure 7.1. From *Cheinet* [2003], a sketched overview of the model including the generation of convective updrafts, the parameterization of their ascent, and the diagnosis of compensating downdrafts.

Furthermore, in his presentation at the AMS Annual Meeting, David New proposed adapting this approach for an ensemble of buoyant thermals, which would allow for scale independence and a more accurate probability distribution of sub-grid turbulence. This approach does not yet include aerosol radiative effects, but it seems likely that aerosols could be introduced into a similar model to attain the most direct simulation yet of their effects on PBL processes. Likewise, evaluating PBL detection methods that use the thermodynamic definition is more straightforward with such a model approach.

Chapter 8. Conclusions

8.1 PBL Detection

The two main techniques for gradient-based PBL detection, wavelet covariance [*Davis et al.*, 2000; *Brooks*, 2003] and simulated annealing [*Steyn et al*., 1999; *Hägeli et al.*, 2000] have complementary strengths and weaknesses, as do different measurement types. The former technique is flexible and simple enough to automate for analyses of long time series and multiple sites, while the latter compensates for noisy signals and low vertical resolution. Both are applicable to the aerosol gradient approximated by lidar backscatter and also the gradient of potential temperature (θ_v) found in thermodynamic profiles. Used together, they make it possible to detect the PBL depth in radiosonde, lidar and infrared spectrometer profiles from the same location and to compare the resulting PBL products. An algorithm combining the two approaches was developed and applied to MPL backscatter, AERI θ_v and radiosonde profile data measured at the Southern Great Plains site over the period of 1996-2004. Intercomparison between AERI- and radiosonde-derived PBL depths shows that the combined algorithm can partly overcome the limitations of the low AERI vertical resolution, with two-thirds of the variation explained by the regression. Unlike MPL and radiosonde, AERI retrievals are unreliable in cloudy conditions. The PBL depth is only detectable in cloud-free profiles.

The intercomparison between MPL- and radiosonde-derived PBL depths is divided into subsets based on cloud conditions and temporal cycling. The algorithm is able to detect the PBL to approximately equal agreement with radiosonde results whether clouds are present or not: in both cases, while there is considerable scatter in the intercomparison, regression R^2 values are above 0.5 and the systematic error is low.

MPL-derived PBL depths are most reliable during times of day when the boundary layer is mature, especially late afternoon, but least reliable during times of transition after dawn and dusk (Figure 8.1). Summertime PBL results are in greater disagreement between backscatter and thermodynamic profiles, likely because deep convection introduces ambiguity to the thermodynamic definition of the PBL. MPL-derived results correctly follow the typical cloud base heights in summer, while radiosonde-derived results may be too high. The MPL instrument at SGP is unable to detect PBLs shallower than 600 m, its overlap range limit.

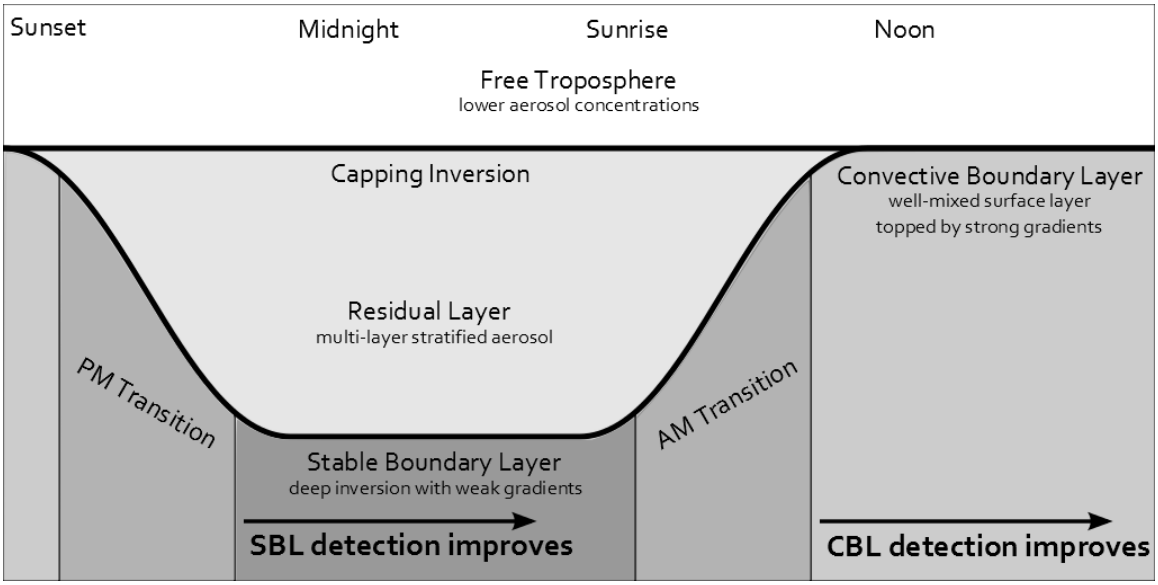

Figure 8.1. Schematic of PBL diurnal cycle with consequences for the detection of boundary-layer regimes.

For the intercomparison between AERI- and radiosonde-derived PBL depths, the results are more complicated. The regression of the full set of PBL results is encouraging, with an R^2 value of 0.67. However, the cluster of comparison points in which the AERI-derived PBL depth is much lower than the radiosonde-derived PBL depth from the same

launch time becomes more significant when the results are broken down by time of day and season. The diurnal cycle of the AERI-derived PBL depth is weak but present when shallow PBLs are included in the analysis, but the seasonal cycle is not resolvable. AERI-derived PBL depths are much too shallow during the summer months, at the same time that radiosonde-derived PBL depths are wildly variable and MPL-derived PBL depths stay close to the typical cloud base depth. The greater sensitivity of the AERI instrument at lower levels may be responsible.

The combined PBL detection algorithm is able to retrieve PBL depths from both remote sensing instruments that correspond well to radiosonde. The differences in the two instruments are even complementary, with AERI best able to find shallow PBL depths that MPL cannot detect, and MPL performing well in cloudy conditions that AERI cannot reliably observe. MPL and AERI-derived PBL depths can therefore be considered accurate at temporal resolutions much higher than the four times daily radiosonde launch, and high-resolution PBL depths may be used for data assimilation and modeling. The detected PBL-to-free-tropospheric transition depths are not reliable, but the more detailed view of diurnal cycling in the PBL is useful in studies of aerosol transport and cloud-aerosol interactions.

The PBL depth results from Chapter 4 of this project are now available as a data product from the ARM archive, and can be found at the following link: http://www.arm.gov/data/pi/84. There is an accompanying research highlight at http://www.arm.gov/science/highlights/RNTA1/view with a brief overview of the method and instruments used in that part of the project. This section of the project is described in full in *Sawyer and Li* [2013]. In addition, work is underway to include the PBL detection

algorithm from Chapter 3 in an upcoming operational data product from ARM, which would provide ongoing PBL depth calculations from several instruments and algorithms to the wider community.

8.2 Comparison to AOD

Because it has been demonstrated that the combined algorithm can reliably detect the PBL depth in MPL profiles without support from other instruments, albeit with known problems in the overnight retrievals, the project is able to compare MPL-based PBL depth retrievals from SGP to those from MPL deployments at sites in China, taking advantage of the full temporal resolution of MPL observations. The HeRO site is especially useful for comparison because the backscatter time series covers six years to SGP's ten, and it is possible to compare their seasonal cycles to one another as well as their diurnal cycles. At SGP, the cyclical changes in PBL depth follow the surface convection: shallow with relatively little change over 24 hours during the winter months, deeper with a clear convective signal in the summer. In the diurnal cycle, the average CBL overtakes the overnight PBL around 10:00 AM local time and reaches its peak at 3:00 PM. This timing of the CBL development holds consistent for the sites at Hefei, Xianghe and Shouxian, as does the shape of the average diurnal cycle; the amplitude of the difference between maximum CBL depth and minimum SBL or RL depth and the overall average height of the PBL top are the factors that change from one site to the next. As models have predicted, differences in AOD do not affect the timing of the CBL

peak; changes in SSA may, but the relatively low AOD values at SGP render the SSA values too uncertain to compare conclusively to the sites in China.

While the seasonal cycle at SGP is relatively predictable, at the HeRO site the interannual variability is strong enough to obscure it entirely. The summer diurnal cycle still shows the strongest signs of surface convection over a 24-hour period, but counter to expectations it is the shallowest on average; deeper PBL depths occur in winter, and there are extended periods in the spring of 2005 and 2007 with very deep PBLs. More detailed synoptic weather data from the site might help to determine whether the changes from one year to the next are due to differences in the monsoon, the Asian dust season, or other causes. In their study at the HeRO site, *Wang et al.* [2014] characterized the changes in AOD with the seasonal cycle; from the patterns they found and the record of PBL depths at Hefei, it can be inferred that higher AOD values disrupt the periodic behavior of the PBL depth and may suppress convection.

The WRF-Chem simulation of April 2004 at SGP is a first step to comparing AOD to PBL depth directly. PBL depths taken at the standard radiosonde launch interval show a weak negative trend with increasing AOD for daytime and early-evening retrievals, with a weaker positive or null trend for the overnight and early-morning retrievals. The trends are qualitatively similar for both the YSU scheme PBL depths calculated by the model and for the PBL depths found by extracting the simulated θ_v profile and using the combined algorithm as if for radiosonde or infrared spectrometer. The same trends are found when actual radiosonde-derived PBL depths are compared to the daily mean AOD values from the modeled period instead, whether using the *Sawyer and Li* [2013] retrievals or the set from *Liu and Liang* [2010]. While the relationship is

only borderline significant and the sample size is too small to quantify the effect with any confidence, it is not dependent on the method used to find the PBL.

Much larger sample sizes are available by comparing the daily mean AOD values to the PBL depth retrievals from the full observation period that coincides with the AOD product. Though AOD observations are never available for the full length of the MPL deployment, the comparison can be made for 2001-2006 at SGP and for 2007-2008 at Hefei. Even exploratory statistics show that the distribution of daily mean PBL depths trends shallower with increasing AOD, with a much more pronounced effect at Hefei because of its greater available range in AOD values. It can also be shown that this trend is limited to the CBL while the overnight SBL and RL retrievals are unaffected; increasing AOD values suppress surface convection, but have no impact on the PBL depth when convection cannot occur.

Probability density functions offer a more detailed analysis of the large data sets. Kernel density estimates show that the CBL depth and AOD distributions form clusters that are specific to certain times of year. While the highest PBL tops at Hefei seem suspicious because of their separation from the rest of the data and the possibility that the cleanest AOD days offer the least MPL backscatter in which to detect the PBL depth, they can be excluded from the data entirely without affecting the conclusion that the daily mean PBL depth decreases with increasing AOD. The rate of decrease as well as the absolute change in PBL depth is much greater at the HeRO site than at SGP. For every unit of increased mean daily AOD, the mean daily PBL depth is roughly 120 m shallower at SGP and 220 m shallower at Hefei (suspicious cluster excluded); this is somewhat greater than previous estimates of the relationship made through model simulations. For

maximum daily PBL depths, which the algorithm detects most reliably, the relationship ranges from a slight increase with AOD at SGP to a decrease of 580 m per unit AOD at Hefei.

It would be helpful in future to expand the study of aerosol-PBL interactions to include the effects of varying SSA, moisture content, and distribution of aerosols through the atmospheric column. There are also modeling approaches that have yet to be applied to this problem. However, this study has already shown that the PBL depth can be detected more accurately and with greater flexibility than was possible using previous methods, and that it interacts with AOD in a way that is consistent with or stronger than the modeled radiative effects. As aerosol emissions increase and the optical depth of aerosol in the atmosphere is enhanced, even aerosols that primarily scatter rather than absorb solar radiation are able to disrupt the energy balance of the lower troposphere, heating the mixed layer at the expense of the surface and enhancing atmospheric stability. This in turn prevents the CBL from reaching its maximum depth over the course of the day, resulting in shallower daily mean PBLs and a reduced volume for the dilution of aerosols and other pollution within the mixed layer. Absorbing aerosol is likely to have a stronger effect than scattering aerosol, and the behavior of boundary-layer convection and cloud layers may change as consequences of the stability within the PBL. Aerosol-PBL interactions must be studied in order to understand the impact of climate change and future emissions on surface air quality, the water cycle and the energy balance within the lower troposphere.

LIST OF REFERENCES

Amiridis, V., et al. (2007), Aerosol lidar observations and model calculations of the planetary boundary layer evolution over Greece, during the March 2006 total solar eclipse, *Atmos. Chem. Phys.*, 7, 6181–6189.

Andreae, M.O., et al. (2004), Smoking rain clouds over the Amazon, *Science*, 303, 1338-1342.

Beyrich, F. and U. Görsdorf (1995), Composing the diurnal cycle of mixing height from simultaneous sodar and wind profiler measurements, *Bound.-Layer Meteor.*, 76, 387-394.

Bianco, L. and J.M. Wilczak (2002), Convective boundary layer depth: Improved measurement by Doppler radar wind profiler using fuzzy logic methods. *J. Atmos. Oceanic Technol.*, 19, 1745-1758.

Bloomer, B. J., et al. (2009), Observed relationships of ozone air pollution with temperature and emissions, *Geophys. Res. Lett.*, 36, L09803, doi:10.1029/2009GL037308.

Brooks, Ian M. (2003), Finding boundary layer top: Application of a wavelet covariance transform to lidar backscatter profiles, *J. Atmos. Oceanic Technol.*, 20, 1092-1105.

Campbell, J.R., et al. (2002), Full-Time, Eye-Safe Cloud and Aerosol Lidar Observation at Atmospheric Radiation Measurement Program Sites: Instruments and Data Processing. *J. Atmos. Oceanic Technol.*, 19, 431-442.

Cheinet, Silvain (2003), A Multiple Mass-Flux Parameterization for the Surface-Generated Convection. Part I: Dry Plumes, *J. Atmos. Sci.*, 60, 2313-2327.

Cheinet, Silvain (2004), A Multiple Mass Flux Parameterization for the Surface-Generated Convection. Part II: Cloudy Cores, *J. Atmos. Sci.*, 61, 1093-1113.

Coulter, R. (2012), *Micropulse Lidar (MPL) Handbook.* U.S. Department of Energy. http://www.arm.gov/publications/tech_reports/handbooks/mpl_handbook.pdf

Davis, K. J., et al. (2000), An objective method for deriving atmospheric structure from airborne lidar observations, *J. Atmos. Oceanic Technol.*, 17, 1455-1468.

Ding, A., et al. (2009), Transport of north China air pollution by midlatitude cyclones: Case study of aircraft measurements in summer 2007, *J. Geophys. Res.*, 114, doi: 10.1029/2009JD012339.

Ding, A., et al. (2013), Intense atmospheric pollution modifies weather: a case of mixed biomass burning with fossil fuel combustion pollution in eastern China. *Atmos. Chem. Phys.*, 13, 10545-10554.

Donnell, E.A., D.J. Fish and E.M. Dicks (2001), Mechanisms for pollutant transport between the boundary layer and the free troposphere, *J. Geophys. Res.*, 106, 7847-7856.

Feingold, G., et al. (2005), On smoke suppression of clouds in Amazonia, *Geophys. Res. Lett.*, 32, L02804, doi:10.1029/2004GL021369.

Feltz, W.F., et al. (1998), Meteorological applications of temperature and water vapor retrievals from the ground-based atmospheric emitted radiance interferometer (AERI). *J. Appl. Meteor.* 37, 857-875.

Feltz, W.F., et al. (2003), Near-continuous profiling of temperature, moisture, and atmospheric stability using the atmospheric emitted radiance interferometer (AERI). *J. Appl. Meteor.* 42, 584-597.

Feltz, W.F., et al. (2007), *Retrieving Temperature and Moisture Profiles from AERI Radiance Observations: AERIPROF Value-Added Product Technical Description.* U.S. Department of Energy. http://www.arm.gov/publications/tech_reports/doe-sc-arm-tr-066.1.pdf?id=168

Fernald, F.G. (1984), Analysis of atmospheric lidar observations: some comments, *Applied Optics* 23, 652-653.

Flynn, Connor J., et al. (2007), "Novel polarization-sensitive micropulse lidar measurement technique." *Optics Express*, 15.6, 2785-2790.

Flynn, C. et al. (2012), *Aerosol Best Estimate (AEROSOLBE) Value-Added Product*. U.S. Department of Energy. http://www.arm.gov/publications/tech_reports/doe-sc-arm-tr-115.pdf?id=472

Garratt, J.R., A.B. Pittock and K. Walsh, 1990. Response of atmospheric boundary layer and soil layer to a high altitude, dense aerosol cover. *J. Appl. Meteor.* 29, 35-52.

Georgoulias, A.K., et al. (2009), Statistical analysis of boundary layer heights in a suburban environment, *Meteorol. Atmos. Phys.* 104, 103-111.

Gentine, Pierre, et al. (2013), A Probabilistic Bulk Model of Coupled Mixed Layer and Convection. Part I: Clear-Sky Case, *J. Atmos. Sci.* 70, 1543-1556.

Hägeli, P., D.G. Steyn and K.B. Strawbridge (2000), Spatial and temporal variability of mixed-layer depth and entrainment zone thickness, *Boundary-Layer Meteorol.*, 97, 47-71.

He, H., et al. (2013), High ozone concentrations on hot days: The role of electric power demand and NO_x emissions, *Geophys. Res. Lett.*, 40, 5291–5294.

Henne, S., et al. (2004), Quantification of topographic venting of boundary layer air to the free troposphere, *Atmos. Chem. Phys.*, 4, 497–509.

Hennemuth, B. and A. Lammert (2006), Determination of the atmospheric boundary layer height from radiosonde and lidar backscatter, *Boundary-Layer Meteorol*. 120, 181-200.

Holdridge, D., et al. (2011), *Balloon-Borne Sounding System (SONDE) Handbook.* U.S. Department of Energy. http://www.arm.gov/publications/tech_reports/handbooks/sonde_handbook.pdf

Hu, X.-M., et al. (2010), Evaluation of three boundary layer schemes in the WRF model, *J. Appl. Meteor. Climatol.*, 49, 1831-1844.

IPCC, 2007. *Climate Change 2007: The Physical Science Basis. Contribution of Working Group I to the Fourth Assessment Report of the Intergovernmental Panel on Climate Change* [Solomon, S., D. Qin, M. Manning, Z. Chen, M. Marquis, K.B. Averyt, M. Tignor and H.L. Miller (eds.)]. Cambridge University Press, Cambridge, United Kingdom and New York, NY, USA.

Jacob, D. J. and D.A. Winner (2009), Effect of climate change on air quality, *Atmos. Env.* 43, 51-63.

Jordan, N.S., et al. (2010), Validation of Goddard Earth Observing System-version 5 MERRA planetary boundary layer heights using CALIPSO, *J. Geophys. Res.*, 115, D24218, doi:10.1029/2009JD013777.

Klett, J.D. (1985), Lidar inversion with variable backscatter/extinction ratios, *Applied Optics* 24, 1638-1643.

Kong, W., and F. Yi (2015), Convective boundary layer evolution from lidar backscatter and its relationship with surface aerosol concentration at a location of a central China megacity, *J. Geophys. Res. Atmos.*, 120, doi:10.1002/2015JD023248.

Law, K.S. and A. Stohl (2007), Arctic air pollution: origins and impacts, *Science*, 315, 1537.

Lewis, J. R., et al. (2013), Improved boundary layer depth retrievals from MPLNET, *J. Geophys. Res.*, 118, 9870-9879.

Li, C., et al. (2010), Transport and evolution of a pollution plume from northern China: A satellite-based case study, *J. Geophys. Res.*, 115, D00K03, doi:10.1029/2009JD012245.

Li, Z., et al. (2011), Long-term impacts of aerosols on the vertical development of clouds and precipitation, *Nature Geoscience* 4, 888-894.

Liu, S. and X.-Z. Liang (2010), Observed diurnal cycle climatology of planetary boundary layer height, *J. Climate*, 23, 5790-5809.

Ma, M., et al. (2011), Characteristics and numerical simulations of extremely large atmospheric boundary-layer heights over an arid region in north-west China, *Boundary-Layer Meteorol.*,140, doi:10.1007/s10546-011-9608-2.

Marenco, F., et al. (1997), Optical properties of tropospheric aerosols determined by lidar and spectrophotometric measurements (Photochemical Activity and Solar Ultraviolet Radiation campaign), *Applied Optics* 36, 6875-6886.

Medeiros, B., A. Hall and B. Stevens (2005), What controls the mean depth of the PBL?, *J. Climate*, 18, 3157-3172.

Melfi, S.H., et al. (1985), Lidar observations of vertically organized convection in the planetary boundary layer over the ocean, *J. Climate Appl. Meteor.*, 24, 806-821.

Nadaraya, E.A. (1963), On estimating regression, *Theory Probab. Appl.*, 9, 141-142.

New, David A. (2015, January), A unified model of the planetary boundary layer and shallow cumulus convection. Paper presented at the AMS Annual Meeting, Phoenix, AZ.

Palm, S., et al. (1998), Inference of marine atmospheric boundary layer moisture and temperature structure using airborne lidar and infrared radiometer data, *J. Appl. Meteor.*, 37, 308-324.

Parikh, N.C. and J.A. Parikh (2002), Systematic tracking of boundary layer aerosols with laser radar, *Optics & Laser Technology*, 34, 177-185.

Park, R.J., et al. (2001), Regional air pollution and its radiative forcing: Studies with a single-column chemical and radiation transport model, *J. Geophys. Res.* 106, 28,751-28,770.

Press, W. H., S. A. Teukolsky, W. T. Vettering, and B. R. Flannery (1992), *Numerical Recipes in FORTRAN: The Art of Scientific Computing*, 2nd ed., Cambridge University Press, pp. 436-447.

Quinn, P. K., et al. (2007), Arctic haze: current trends and knowledge gaps. *Tellus* 59B, 99-114.

Rio, Catherine, et al. (2013), Control of deep convection by sub-cloud lifting processes: the ALP closure in the LMDZ5B general circulation model, *Clim. Dyn.* 40, 2271–2292.

Sawyer, V.R. and Z. Li (2013), Detection, variations and intercomparison of the planetary boundary layer depth from radiosonde, lidar and infrared spectrometer, *Atmos. Env.* 79, 518-528.

Seibert, P., et al. (2000), Review and intercomparison of operational methods for the determination of the mixing height, *Atmos. Environ.*, 34, 1001-1027.

Seinfeld, John H. and Spyros N. Pandis (2006), *Atmospheric Chemistry and Physics: from Air Pollution to Climate Change*, 2nd ed., WileyBlackwell, Hoboken, N.J.

Sivaraman, C. and J. Comstock (2011), *Micropulse Lidar Cloud Mask Value-Added Product Technical Report*. U.S. Department of Energy. http://www.arm.gov/publications/tech_reports/doe-sc-arm-tr-098.pdf

Spinhirne, J.D., et al. (1995), "Compact Eye Safe Lidar Systems," *Rev. Laser Eng.*, 23, 112-118.

Spinhirne, James D (1993), "Micro pulse lidar." *Geoscience and Remote Sensing, IEEE Transactions* 31.1 (1993): 48-55.

Steyn, D.G., M. Baldi and R.M. Hoff (1999), The detection of mixed layer depth and entrainment zone thickness from lidar backscatter profiles, *J. Atmos. Ocean. Technol.*, 16, 953-959.

Stull, Ronald B. (1988), *An Introduction to Boundary Layer Meteorology*, Springer-Verlag New York, LLC.

Sun, Y., et al. (2010), Asian dust over northern China and its impact on the downstream aerosol chemistry in 2004, *J. Geophys. Res.*, 115, D00K09, doi:10.1029/2009JD012757.

Tskaknakis, G. et al. (2011), Inter-comparison of lidar and ceilometer retrievals for aerosol and Planetary Boundary Layer profiling over Athens, Greece, *Atmos. Meas. Tech.* 4, 1261–1273.

Twohy, C.H., et al. (2002), Deep convection as a source of new particles in the midlatitude upper troposphere, *J. Geophys. Res.*, 107, D21, doi: 10.1029/2001JD000323.

Venkatram, A. and R. Viskanta (1977), Effects of aerosol-induced heating on the convective boundary layer. *J. Atmos. Sci.*, 34, 1918-1933.

Wang, Z., and K. Sassen (2001), Cloud Type and Macrophysical Property Retrieval Using Multiple Remote Sensors, *J. Appl. Meteor.*, 40, 1665-1682.

Wang, Z. et al. (2014), Seasonal characteristics of aerosol optical properties at the SKYNET Hefei site (31.90°N, 117.17°E) from 2007 to 2013, *J. Geophys. Res. Atmos.*, 119, 6128–6139, doi:10.1002/2014JD021500.

Watson, G.S. (1964), Smooth regression analysis, *Sankhyā: The Indian Journal of Statistics, Series A,* 26, 359-372.

Welton, E. J., et al. (2001), Global monitoring of clouds and aerosols using a network of micro-pulse lidar systems, in *Lidar Remote Sensing for Industry and Environmental Monitoring*, U. N. Singh, T. Itabe, N. Sugimoto, (eds.), Proc. SPIE, 4153, 151-158.

Xing, J., et al. (2015, January), Air pollution and climate response to aerosol direct radiative effects: a modeling study of decadal trends across the northern hemisphere. Paper presented at the AMS Annual Meeting, Phoenix, AZ.

Yang, X., M. Ferrat, and Z. Li (2013a), New evidence of orographic precipitation suppression by aerosols in central China, *Meteorol. Atmos. Phys*., doi:10.1007/s00703-012-0221-9.

Yang, X., Z. Yao**,** Z. Li, and T. Fan (2013b), Heavy air pollution suppresses summer thunderstorms in central China, *J. Atmos. Sol-Terr. Phy.*, 95-96, 28-40.

Yu, H., S. C. Liu and R. E. Dickinson, 2002. Radiative effects of aerosols on the evolution of the atmospheric boundary layer. *J. Geophys. Res.* 107, doi:10.1029/2001JD000754.

Zhang, Y., X.-Y. Wen and C.J. Jang (2010), Simulating chemistry-aerosol-cloud-radiation-climate feedbacks over the continental U.S. using the online-coupled Weather Research Forecasting Model with chemistry (WRF/Chem), *Atmos. Env.*, 44, 3568-3582.